Resource

Cell

Single-Cell Transcriptomic Atlas of Primate Ovarian Aging

Graphical Abstract

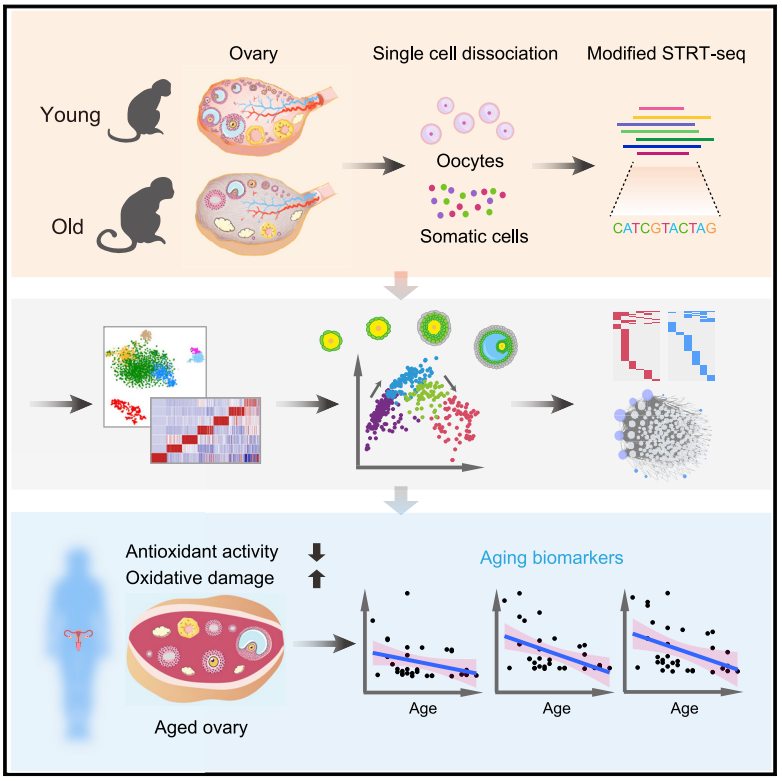

Authors

Si Wang, Yuxuan Zheng, Jingyi Li, ..., Jing Qu, Fuchou Tang, Guang-Hui Liu

Correspondence

belmonte@salk.edu (J.C.I.B.), qujing@ioz.ac.cn (J.Q.), tangfuchou@pku.edu.cn (F.T.), ghliu@ioz.ac.cn (G.-H.L.)

In Brief

Single-cell transcriptomic analysis in ovaries of young and old cynomolgus monkeys identifies aging-associated and cell-type-specific dysregulation of antioxidative pathways.

Highlights

- Single-cell transcriptomic roadmap of NHP ovarian aging
- Molecular signatures revealed for NHP oocytes at stepwise developmental stages
- Cell-type-specific inactivation of antioxidant genes in aged monkey and human ovaries

Wang et al., 2020, Cell *180*, 585–600
February 6, 2020
https://doi.org/10.1016/j.cell.2020.01.009

CellPress

Resource

Cell

Single-Cell Transcriptomic Atlas of Primate Ovarian Aging

Si Wang,[1,3,4,5,7,16] Yuxuan Zheng,[2,9,10,16] Jingyi Li,[1,4,5,7,16] Yang Yu,[6,12,16] Weiqi Zhang,[4,5,7,8,13,16] Moshi Song,[1,7,8,15] Zunpeng Liu,[3,7] Zheying Min,[6] Huifang Hu,[3,7] Ying Jing,[3,7] Xiaojuan He,[5] Liang Sun,[14] Lifang Ma,[6] Concepcion Rodriguez Esteban,[11] Piu Chan,[5,15] Jie Qiao,[6,15] Qi Zhou,[3,7,8,15] Juan Carlos Izpisua Belmonte,[11,*] Jing Qu,[3,7,8,*] Fuchou Tang,[2,9,10,*] and Guang-Hui Liu[1,4,5,7,8,17,*]

[1]State Key Laboratory of Membrane Biology, Institute of Zoology, Chinese Academy of Sciences, Beijing 100101, China
[2]Beijing Advanced Innovation Center for Genomics, College of Life Sciences, Peking University, Beijing 100871, China
[3]State Key Laboratory of Stem Cell and Reproductive Biology, Institute of Zoology, Chinese Academy of Sciences, Beijing 100101, China
[4]National Laboratory of Biomacromolecules, CAS Center for Excellence in Biomacromolecules, Institute of Biophysics, Chinese Academy of Sciences, Beijing 100101, China
[5]Beijing Institute for Brain Disorders, Advanced Innovation Center for Human Brain Protection, National Clinical Research Center for Geriatric Disorders, Xuanwu Hospital Capital Medical University, Beijing 100053, China
[6]Department of Obstetrics and Gynecology, Center for Reproductive Medicine, Peking University Third Hospital, Beijing 100191, China
[7]University of Chinese Academy of Sciences, Beijing 100049, China
[8]Institute for Stem cell and Regeneration, CAS, Beijing 100101, China
[9]Biomedical Institute for Pioneering Investigation via Convergence, Ministry of Education Key Laboratory of Cell Proliferation and Differentiation, Beijing 100871, China
[10]Peking-Tsinghua Center for Life Sciences, Academy for Advanced Interdisciplinary Studies, Peking University, Beijing 100871, China
[11]Gene Expression Laboratory, Salk Institute for Biological Studies, La Jolla, California, United States of America
[12]Stem Cell Research Center, Peking University Third Hospital, Beijing 100191, China
[13]Disease Genomics and Individualized Medicine Laboratory, Beijing Institute of Genomics, Chinese Academy of Sciences, Beijing 100101, China
[14]The MOH Key Laboratory of Geriatrics, Beijing Hospital, National Center of Gerontology, Beijing 100730, China
[15]Senior author
[16]These authors contributed equally
[17]Lead Contact
*Correspondence: belmonte@salk.edu (J.C.I.B.), qujing@ioz.ac.cn (J.Q.), tangfuchou@pku.edu.cn (F.T.), ghliu@ioz.ac.cn (G.-H.L.)
https://doi.org/10.1016/j.cell.2020.01.009

SUMMARY

Molecular mechanisms of ovarian aging and female age-related fertility decline remain unclear. We surveyed the single-cell transcriptomic landscape of ovaries from young and aged non-human primates (NHPs) and identified seven ovarian cell types with distinct gene-expression signatures, including oocyte and six types of ovarian somatic cells. In-depth dissection of gene-expression dynamics of oocytes revealed four subtypes at sequential and stepwise developmental stages. Further analysis of cell-type-specific aging-associated transcriptional changes uncovered the disturbance of antioxidant signaling specific to early-stage oocytes and granulosa cells, indicative of oxidative damage as a crucial factor in ovarian functional decline with age. Additionally, inactivated antioxidative pathways, increased reactive oxygen species, and apoptosis were observed in granulosa cells from aged women. This study provides a comprehensive understanding of the cell-type-specific mechanisms underlying primate ovarian aging at single-cell resolution, revealing new diagnostic biomarkers and potential therapeutic targets for age-related human ovarian disorders.

INTRODUCTION

The ovary is a critical female reproductive organ, serving as the source of oocytes and major supplier of steroid sex hormones (Rimon-Dahari et al., 2016). Thus, the ovary is indispensable for both the maintenance of female fertility and endocrine homeostasis. The ovary is one of the organs that exhibit early-onset aging-associated dysfunction in human, with evident declines after only 30 years of age (Broekmans et al., 2009; Tilly and Sinclair, 2013). Age-associated decreases of follicle number and oocyte quality result in female fertility decline (Perheentupa and Huhtaniemi, 2009). Menopause is the natural consequence of ovarian physiological aging (Colman, 2018; Li et al., 2012). Other disorders, such as ovarian cancer, type 2 diabetes mellitus, and breast cancer could also be related to ovarian aging (Perry et al., 2015; Webb and Jordan, 2017). Therefore, an in-depth understanding of the mechanisms driving ovarian aging is of critical importance.

The ovary is a complex structure consisting of numerous heterogeneous cell types at various stages, including follicles at different developmental stages. Each follicle is comprised of an oocyte, surrounding granulosa cells and/or theca cells

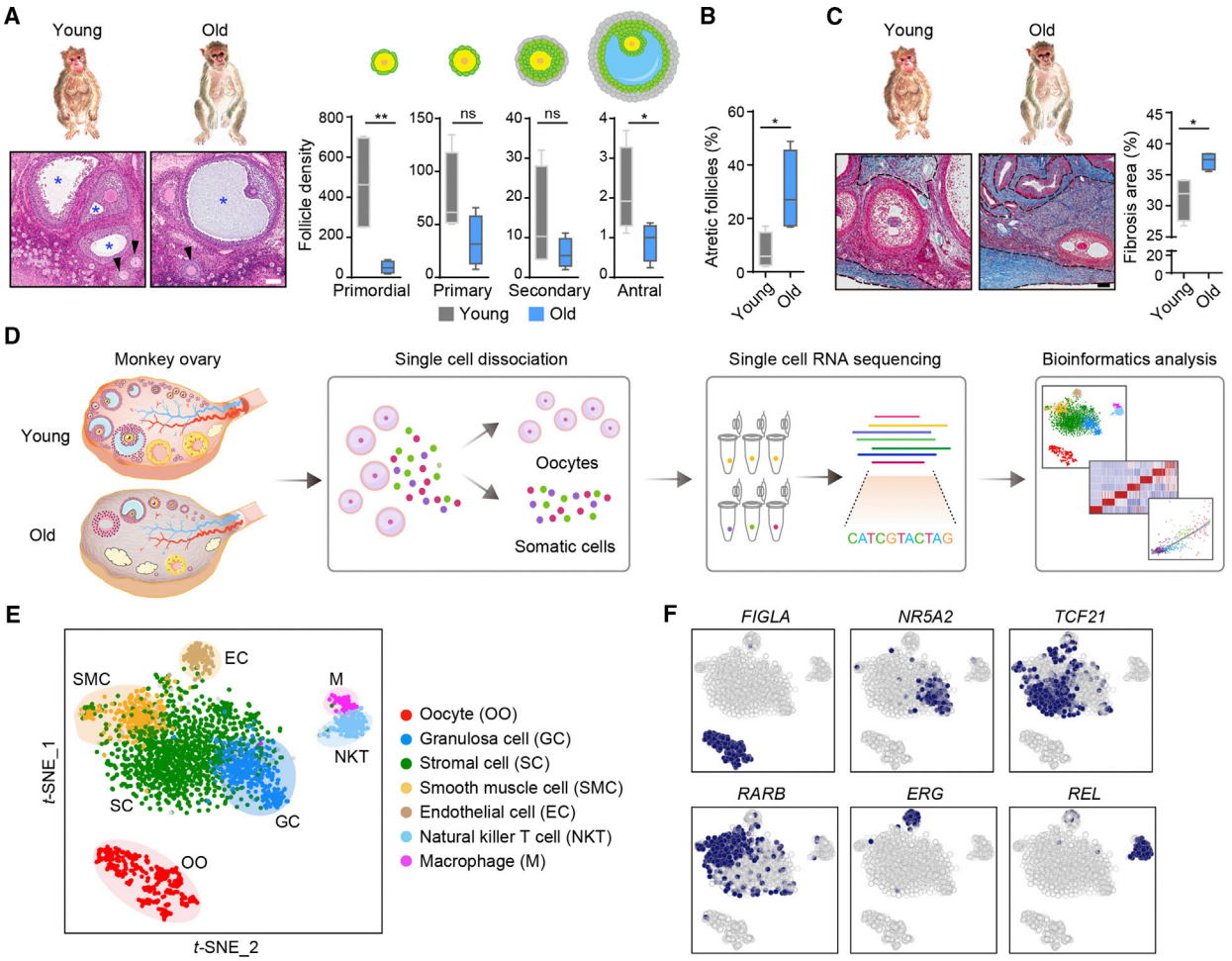

(legend on next page)

(Sánchez and Smitz, 2012). They are generally scattered throughout the ovarian cortex, moving into the medulla during maturation. Besides the reductions in follicle number, other aging-associated anatomical and physiological changes include increased fibrosis, expanded stromal cell compartment, and changed medullary and cortex volume (Nicosia, 1987; Walker et al., 2009).

For a heterogeneous organ such as the ovary, conventional bulk RNA-sequencing (RNA-seq) approaches have difficulties in accurately revealing cell-type-specific changes in gene expression, particularly for rare cell types. With advances in the single-cell RNA sequencing (scRNA-seq) technique, it is now possible to analyze alterations in gene transcription within highly heterogeneous tissues at single-cell level (Baryawno et al., 2019; Cao et al., 2019; Su et al., 2018). Of note, modified single-cell tagged reverse transcription (STRT) technique enables multiplexed single-cell RNA-seq with detection of abundant genes per cell, especially for fewer cells (Cui et al., 2019; Islam et al., 2011).

Due to ethical constraints and limited access to disease-free human ovarian tissues, a non-human primate (NHP) sharing similar genetic and physiological features with humans, makes an ideal model for studying ovarian aging and dysfunction (Anderson and Colman, 2011; Bellino and Wise, 2003; Walker and Herndon, 2008; Zhang et al., 2018a). Additionally, their ovarian morphological characteristics, menstrual cycle, and patterns of sex hormone secretion are similar to human ovaries (Bellino and Wise, 2003). Importantly, the aging characteristics of NHP ovaries are also similar to those in humans (Walker and Herndon, 2008). To date, however, scRNA-seq has not been used to systematically characterize the NHP ovary (including oocytes and ovarian somatic cells), and the effect of aging on various ovarian cell types in primates has not been analyzed in depth either.

In this study, we used cynomolgus monkeys to survey the first comprehensive single-cell transcriptomic landscape of ovarian aging. We identified gene-expression signatures for seven ovarian cell types and mapped the unique transcriptional landscape of four oocyte subtypes during folliculogenesis by scRNA-seq. Moreover, aging-associated gene-expression changes revealed that oxidative damage was an essential factor of ovarian aging. Analysis of human granulosa cells revealed similar aging-associated downregulation of antioxidant genes and knockdown of these genes compromised oxidative stress responses. These data indicate that the functional decay of cell-type-specific redox regulatory networks has profound effects on ovarian aging, providing potential biomarkers for the clinical diagnosis of ovarian aging and targets for developing novel therapeutic interventions to treat aging-associated ovarian disorders and female infertility.

RESULTS

Diminished Follicle Reserve in Aged Ovaries from Cynomolgus Monkeys

We obtained ovaries from four juvenile (4–5 years old) and four aged (18–20 years old) cynomolgus monkeys (Appt et al., 2010; Drevon-Gaillot et al., 2006) (Figure S1A). As species of the genus *Macaca* undergo menopause at approximately 25 years of age (Colman, 2018; Kavanagh et al., 2005; Walker and Herndon, 2008), the aged monkeys analyzed here were in the period of pre-menopause or peri-menopause and thus suitable for studying ovarian aging. Histologically, the ovaries collected from aged monkeys had fewer follicles at each developmental stage (primordial, primary, secondary, and antral follicles) than those collected from young monkeys (Figure 1A). Notably, aged ovaries had a higher percentage of atretic follicles than did young ovaries (Figures 1B and S1B). These results revealed an aging-associated decline in ovarian follicle reserves and an accelerated loss of primordial follicle pool during aging, as reported (Nichols et al., 2005). In addition, increased ovarian fibrosis was observed in the stroma of aged ovaries (Figure 1C).

Single-Cell Transcriptome Profiling of Monkey Ovaries Identified Different Ovarian Cell Types and Gene Expression Signatures

To investigate the cell-type-specific alterations in gene expression during ovarian aging at single-cell resolution, we subjected ovaries from cynomolgus monkeys to scRNA-seq analysis by using the modified STRT technique (Figure 1D). For these analyses, we roughly divided the ovary into cortex and medulla before enzymatic digestion (Figure 1D). After stringent cell filtration, the high-quality transcriptomes of 2,601 single cells (418 oocytes and 2,183 somatic cells) collected from four young and four aged individuals were retained for subsequent analyses (Figure S1C; Table S1). To

Figure 1. Distinct Ovarian Cell Subpopulations with Transcriptional Signatures Determined by Single-Cell RNA-Seq Analysis of Monkey Ovaries

(A) Left: hematoxylin and eosin (H&E)-stained sections of young and old monkey ovaries. Arrowheads and asterisks denote secondary and antral follicles, respectively. Right: density quantification of different stages of follicles indicated by the morphology shown by the cartoons. Scale bar, 100 μm. n = 4 monkeys. ns, not significant, *p < 0.05 and **p < 0.01 (one-tailed t test).

(B) Percentage of atretic follicles to total follicles based on H&E-stained sections. n = 4 monkeys. *p < 0.05 (two-tailed t test).

(C) Masson's trichrome staining of young and old monkey ovaries. Dashed lines denote fibrosis areas. Scale bar, 100 μm. n = 4 monkeys. *p < 0.05 (two-tailed t test).

(D) Flowchart overview of monkey ovarian scRNA-seq.

(E) *t*-SNE plot showing seven ovarian cell types.

(F) *t*-SNE plots characterizing representative transcriptional regulators for different cell types. Blue color denotes the cells with the activation of indicated transcriptional regulators.

(G) *t*-SNE plots showing expression levels of oocyte and somatic cell marker genes.

(H) Left: heatmap showing expression signatures of top 50 specifically expressed genes in each cell type; the value for each gene is row-scaled *Z* score. Right: representative GO terms.

See also Figures S1 and S2; Table S1.

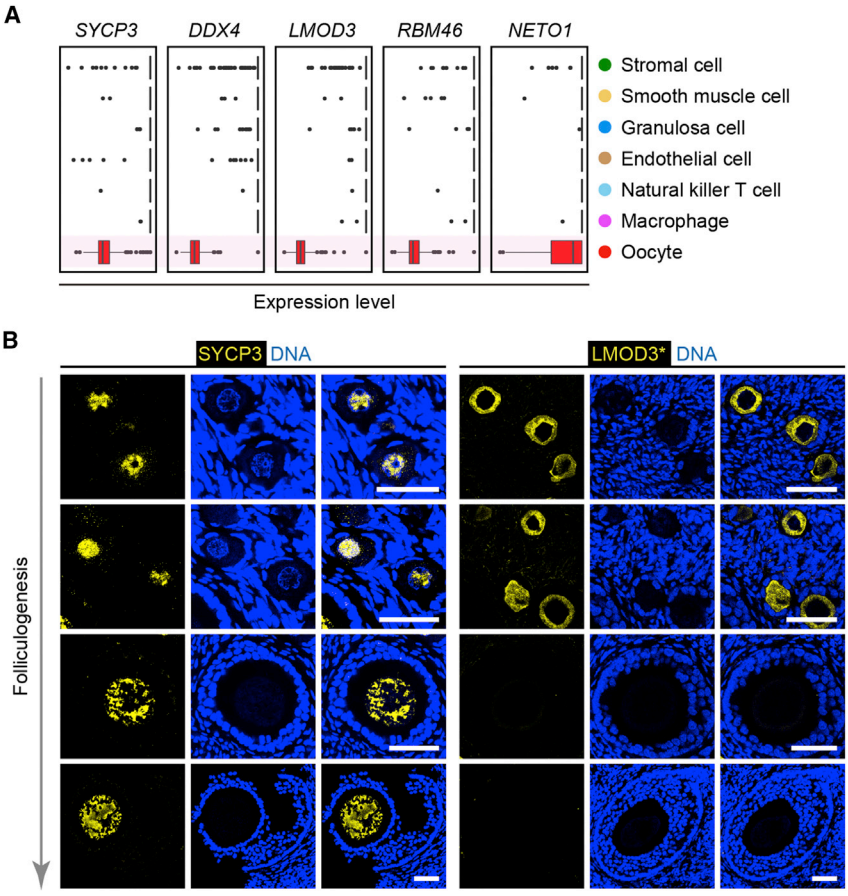

Figure 2. Single-Cell RNA Expression Survey of Oocytes in Monkey

(A) Boxplots showing representative oocyte-specific markers.

(B) Immunofluorescence analysis of SYCP3 and LMOD3 in monkey oocytes. Asterisk represents the newly identified oocyte marker LMOD3. Scale bar, 50 μm.

See also Figure S2; Table S1.

characterize ovarian cell types, we performed single-cell regulatory network inference and clustering (SCENIC) analysis to score the activity of gene regulatory networks in each single cell to identify the stable cell states (Aibar et al., 2017; Davie et al., 2018). Modules with genes co-expressed with transcription factors (TFs) were first established, and *cis*-regulatory motif analysis was applied to select significantly enriched modules for scoring the activity of subnetworks. We then performed *t*-distributed stochastic neighbor embedding (*t*-SNE) dimensionality analysis according to the subnetwork activity information obtained from SCENIC analysis and revealed seven main cell types by unsupervised clustering analysis (Figure 1E) (Lake et al., 2016). Global transcriptomic profiling showed no significant differences in ovarian cell type distribution among monkeys of different ages, indicating that these cell types reflected physiological differences between cells, rather than technical variations or the effect of genetic backgrounds (Figure S1D). SCENIC analysis revealed several important transcriptional regulators modulating cell-type-specific gene regulatory networks, such as *FIGLA* for oocytes (OOs), *NR5A2* for granulosa cells (GCs), and *TCF21* for stromal cells (SCs) (Figure 1F) (Meinsohn et al., 2017; Soyal et al., 2000; Stevant et al., 2019). To further identify these cell clusters, we mapped the gene-expression profiles of well-defined cell-type-specific markers in the *t*-SNE plot (Figures 1G and S1E). Accordingly, seven cell clusters were identified, including oocyte and six types of ovarian somatic cells (Figures 1E and 1H; Table S1).

A cluster corresponding to oocytes was identified based on the expression of oocyte-specific markers, such as *SYCP3* (essential for meiosis) (Prieto et al., 2004), *DDX4* and *GDF9* (essential for oocyte development) (Castrillon et al., 2000; Dong et al., 1996), and *ZP3* (essential for the composition of the zona pellucida) (Figures 1G, 2A, and S1E) (Ringuette et al., 1986). Localization of SYCP3 and DDX4 to these cells was confirmed via immunofluorescence imaging (Figures 2B and S2A). Besides these classic markers, we identified a panel of novel markers for oocytes, including LMOD3 that was primarily expressed in the oocytes of primordial and primary follicles (Figures 2A and 2B), and RBM46 and NETO1 (Figures 2A and S2A) that were dominantly expressed in oocytes at different stages of folliculogenesis.

A cluster corresponding to GCs was identified by the expression of classic markers *AMH*, *WT1*, and *INHA* (Figures 1G and S1E) (Rimon-Dahari et al., 2016). Notably, some cells in this cluster expressed a mural granulosa cell marker *CYP19A1* (Stocco, 2008) (Figure S1E). WT1 was detected in GCs in follicles of each stage, whereas AMH was primarily detected in GCs of antral follicles by immunostaining (Figures S2B and S2C), similar to the expression pattern of AMH in human ovaries (Zhang et al., 2018b).

Stromal cell (SC) markers, *TCF21* and *COL1A2*, were specifically expressed in one cluster (Figures 1G and S1E) (Hatzirodos et al., 2015). Interestingly, some cells in this cluster expressed high levels of the theca marker *STAR* (Figures 1G and S2D), implying that this cluster contained theca cells that are associated with the development and maturation of follicles (Magoffin, 2005). Smooth muscle cells (SMCs) and endothelial cells (ECs) were identified by SMC markers *DES* and *ACTA2*, and EC markers *CDH5* and *VWF*, respectively (Figures 1G, S1E, and S2E) (Owens et al., 2004; Randi et al., 2018). Immune cells, such as natural killer T cells (*CD3D*- and *KLRB1*-positive) and macrophages (*CD68*- and *CD14*-positive), were also captured in the scRNA-seq dataset (Figures 1G and S1E) (Kurioka

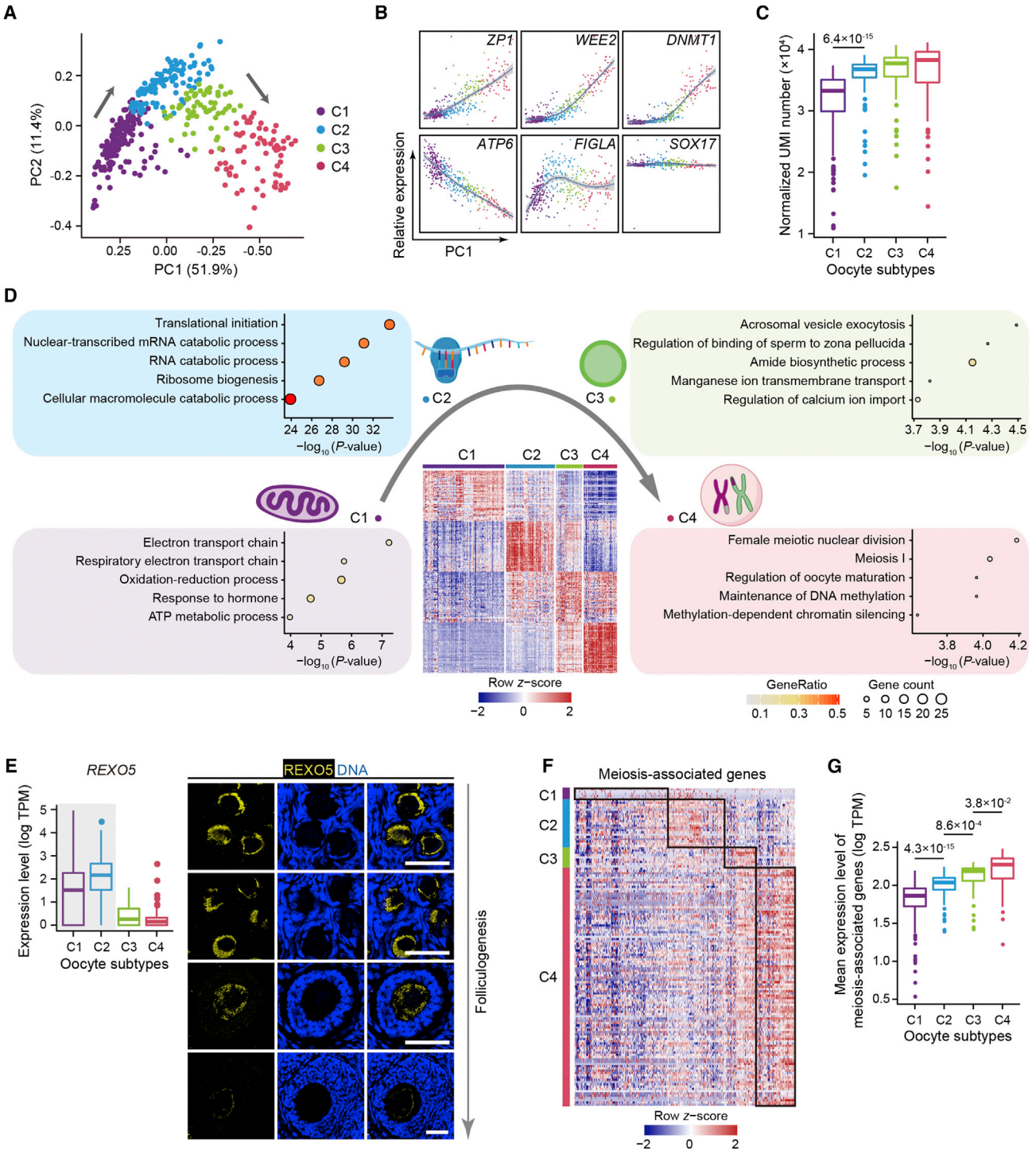

Figure 3. Dynamic Gene-Expression Patterns of Oocyte Subtypes at Stepwise Developmental Stages

(A) PCA plot showing four oocyte subtypes based on gene-expression patterns exhibited by PC1 and PC2.

(B) Relative gene-expression patterns of representative genes essential for oocyte development along the PC1 dimension.

(C) Boxplot showing the normalized UMI number in each oocyte subtype. The two-tailed t test p value is indicated.

(D) Heatmap showing scaled expression levels of top 50 subtype-specific genes in four oocyte subtypes. Representative GO terms for stage-specific genes are shown.

(legend continued on next page)

et al., 2018; Sousa et al., 2015). Finally, we found that GCs and SCs were mostly from the ovarian cortex whereas SMCs and immune cells were mainly from the ovarian medulla (Figure S1D), consistent with the enrichment strategy and ovarian anatomy.

We next analyzed the biological function of each cell cluster by using Gene Ontology (GO) analysis of differentially expressed genes (DEGs) (Figure 1H; Table S1), revealing unique characteristics of these NHP ovarian cells. For example, GO terms specific to oocytes included "meiotic cell cycle" and "gamete generation." GO terms including "anti-Müllerian hormone signaling pathway" and "reproductive structure development" were enriched for GCs. GO terms including "extracellular matrix organization" and "blood vessel development" were enriched for SCs, suggesting that SCs provide structural and nutritional support for ovarian tissue (Rimon-Dahari et al., 2016). Collectively, we identified seven different ovarian cell types, including oocyte and ovarian somatic cells, and depicted gene-expression signatures for each cell type, including novel markers for oocytes.

Unique Gene-Expression Signatures of Four Subtypes of Oocytes at Sequential and Stepwise Developmental Stages

To explore the gene-expression dynamics of oocytes during folliculogenesis, we performed unsupervised analysis of oocyte gene-expression profiling and identified four subtypes of oocytes (C1 to C4). Principal component analysis (PCA) revealed that the four oocyte subtypes were distributed along the principal component 1 (PC1) dimension (Figure 3A; Table S2). Consistently, the relative expression levels of genes known to be essential for follicular development also varied along PC1 axis (Figures 3B and S3A). Genes promoting follicle development, such as *ZP1*, *BMP15*, and *GDF9*, were progressively upregulated from oocyte subtype C1 to C4. Meiotic M phase genes *WEE2* and *AURKA* as well as DNA methyltransferase, *DNMT1* and *DNMT3A*, were also gradually upregulated from subtype C1 to C4 (Figures 3B and S3A). On the contrary, *ATP6* and *COX2* were highly expressed in primordial follicles, as previously described (Markholt et al., 2012), and were progressively downregulated from subtype C1 to C4 (Figures 3B and S3A). These results demonstrate that the PC1 dimension traced the sequential and stepwise developmental trajectory of oocytes. In addition, consistent with the increased levels of detected transcript abundance in oocytes of growing follicles post recruitment (Gu et al., 2019; Sha et al., 2019), the number of transcripts (based on spike-in-normalized unique molecular identifier [UMI]) and the number of genes detected in each individual cell progressively increased from subtype C1 to C4 (Figures 3C and S3B). Therefore, we inferred that oocytes in subtypes C1, C2, C3, and C4 were from primordial, primary, secondary, and antral follicles, respectively.

We next dissected the regulatory pathways involved in folliculogenesis by performing GO analysis of genes specific for a particular oocyte cluster (i.e., stage) (Figure 3D; Table S2). In line with the previous reports and the above canonical gene-expression patterns, GO analysis revealed the biological processes that were enriched for each stage of follicular development (Figure 3D). Notably, "electron transport chain" and "ATP metabolic process" were enriched in subtype C1 with high expression of mitochondria-related genes (representative genes *MT-ND2* and *MT-ND4*) (Table S2), which were supported by high expression levels of TOM20 and ND1 in primordial follicles via immunofluorescence labeling (Figure S3C). In addition, "translational initiation" and "ribosome biogenesis" were enriched in subtype C2 with increased expression of ribosome-related genes (representative genes *RPL23A* and *RPL24*) (Table S2). We also identified a new marker highly expressed in early-stage oocytes, REXO5, which is a newly identified RNA exonuclease that plays a crucial role in ribosome biogenesis (Figure 3E) (Gerstberger et al., 2017). Interestingly, "acrosomal vesicle exocytosis (representative genes *ZP3* and *ZP4*)" and "regulation of calcium ion import (representative genes *CALM2* and *ATP2C2*)" were enriched in subtype C3 (Table S2). Finally, "meiosis I" was enriched in subtype C4 with high expression levels of *AURKA* and *WEE2*. "Maintenance of DNA methylation" and "methylation-dependent chromatin silencing" were also enriched in subtype C4 with high expression levels of *UHRF1* and *DNMT1* (Table S2). We next investigated the expression patterns of "meiosis-related genes" in oocytes. A total of 197 mammalian genes involved in meiosis were gathered from the *Macaca fascicularis* annotated reference genome (Table S3) (Bult et al., 2019; Harris et al., 2004). Among these genes, 140 were differentially expressed across different stages of oocyte development, with the mean expression progressively increasing in oocytes as the follicle progressed from primordial to antral stage (Figures 3F and 3G).

To analyze gene-expression changes involved in each stage-to-stage transition during folliculogenesis, we identified DEGs in comparisons between consecutive stages (Figures S3D and S3E; Table S2). The most dramatic increase in the number of upregulated genes occurred during the transition of oocytes from secondary to antral follicles (C3 to C4). To identify the master regulators of folliculogenesis, we constructed transcriptional regulatory networks of core transcriptional regulators and their target genes. Stage-specific regulatory networks revealed a core hub of genes that regulated the cell-type-specific markers at each stage of oocyte development, including *ELF4* and *FOS* in oocytes from primordial follicles, *RPS4X* and *FIGLA* in oocytes from primary follicles, *SPAG7* and *TAF1A* in oocytes from secondary follicles, and *HMGB3* and *CCDC25* in oocytes from antral follicles (Figure S3F). Altogether, our results reveal the full continuum of gene-expression programs and stage-specific transcriptional regulatory networks underlying folliculogenesis in NHPs.

(E) Boxplot (left) and immunofluorescence analysis (right) of the novel marker REXO5 highly expressed in early stage oocytes. Scale bar, 50 μm.
(F) Heatmap showing scaled expression levels of meiotic genes differentially expressed among oocyte subtypes.
(G) Boxplot showing mean expression levels of meiotic genes in each oocyte subtype. Two-tailed t test p values are indicated.
See also Figure S3; Tables S2 and S3.

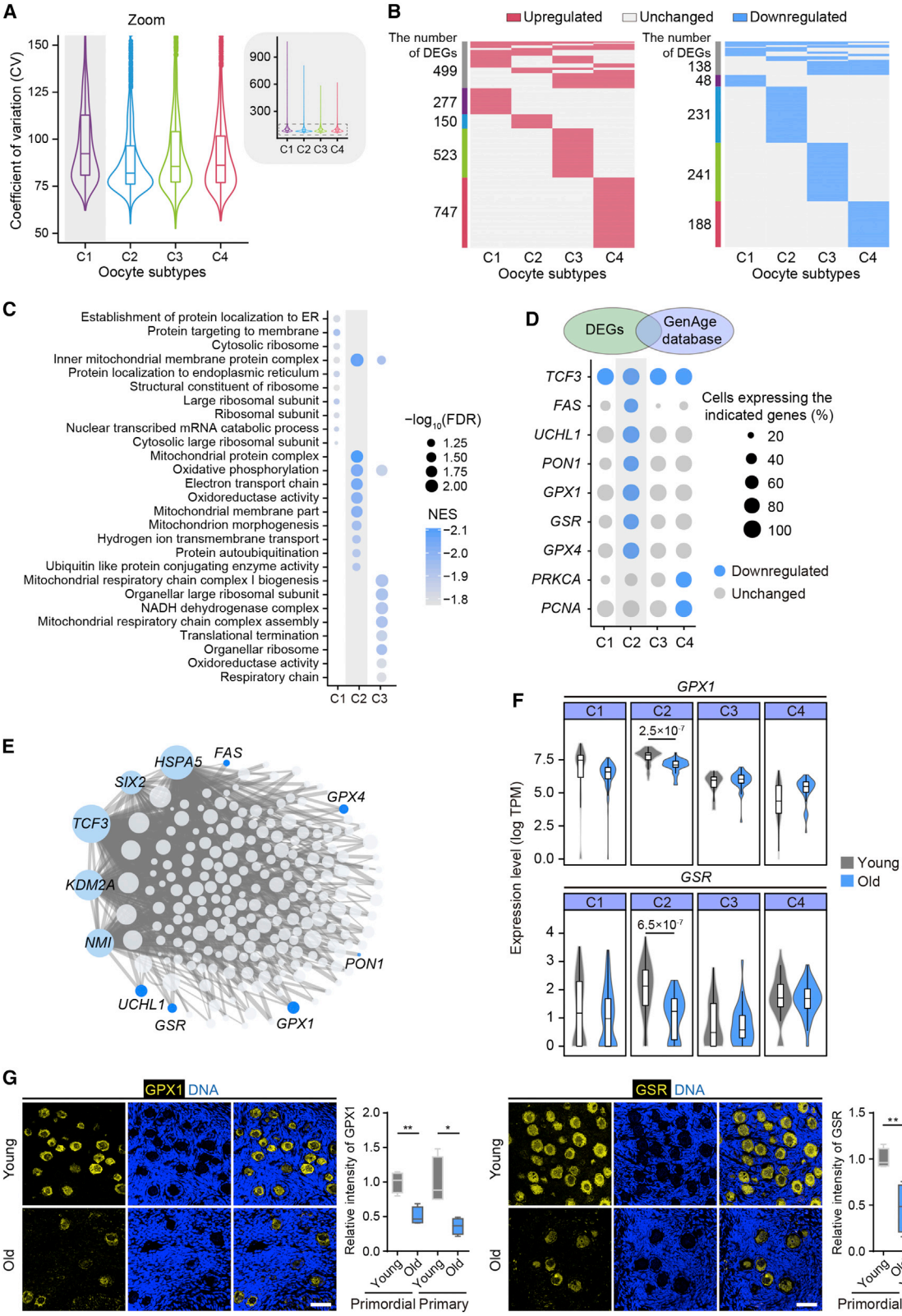

(legend on next page)

Downregulation of Antioxidant Genes in Aged Early-Stage Oocytes

We next sought to identify aging-associated changes in gene expression in ovarian cells. SCENIC analysis revealed the evenly distributed cell populations along with similarly expressed cell-type-specific marker genes in young and aged ovaries, indicating that aging had minimal effect on ovarian cell identity (Figures S1D and S4A). Furthermore, hotspot genes annotated in the GenAge database of aging/longevity-related genes and in the datasets for ovarian diseases including premature ovarian failure (POF) and primary ovarian insufficiency (POI) (Table S3) (Cordts et al., 2011; de Magalhães et al., 2009; Rossetti et al., 2017) were mainly expressed in oocytes, GCs, and SCs (Figures S4B and S4C), suggesting that these cell types were important to ovarian homeostasis and aging.

Calculation of age-relevant coefficient of variation (CV) revealed that oocytes from primordial follicles exhibited higher transcriptional noise than that of oocytes from late-stage follicles (Figure 4A) (Salzer et al., 2018), indicating that aging caused higher variability in oocytes from early-stage follicles than those from late-stage follicles. Further analysis revealed 534, 335, 864, and 1,068 upregulated DEGs, and 106, 286, 346, and 278 downregulated DEGs in old versus young oocyte subtypes C1, C2, C3, and C4, respectively (Figure 4B; Table S4). Notably, most of these aging-associated DEGs were subtype-specific, with only 14 upregulated and six downregulated shared by all four oocyte subtypes, indicative of the oocyte subtype-specific effects of aging. Only modest expression changes were observed in development-specific genes for each oocyte subtype, such as meiosis-related genes (Figure S4D). In addition, GO analysis based on gene set enrichment analysis (GSEA) revealed the aging-associated alterations in cellular function of each oocyte subtype (Figures 4C and S4E). Particularly, several genes in "oxidative phosphorylation" and "oxidoreductase activity" pathways were downregulated in oocyte subtype C2 (Figure 4C).

Comparative analysis of aging-associated DEGs of different oocyte subtypes with the aging/longevity-associated genes annotated in the GenAge database (Figures 4D and S4F) revealed a possible link between decreased antioxidant defense of oocyte subtype C2 and ovarian aging, as evidenced by the oocyte subtype C2-specific downregulation of several genes related to oxidative stress response, including *GPX1* [$\log_2$(fold change) = −1.04, p value = 6.5×10^{-7}], *GSR* [$\log_2$(fold change) = −1.04, p value = 6.5×10^{-7}], *GPX4* [$\log_2$(fold change) = −0.53, p value = 0.003], and *PON1* [$\log_2$(fold change) = −0.60, p value = 0.015] (Figure 4D). Transcriptional regulatory network analysis of aging-associated downregulated DEGs of oocyte subtype C2 further revealed *TCF3*, *HSPA5*, *KDM2A*, *SIX2*, and *NMI* as the top 5 master regulators (Figure 4E). Similarly, different hub genes constituted the stage-specific aging-associated DEG regulatory networks responsible for the altered gene-expression patterns during aging (Figures S5A and S5B). Consistent with the detected changes in mRNA levels, immunostaining analyses confirmed decreased GPX1 and GSR protein levels in oocytes from early-stage follicles in aged ovaries (Figures 4F and 4G). Altogether, these findings suggest that the downregulation of antioxidant genes, including *GPX1* and *GSR*, is a unique aging feature of early-stage oocytes, likely contributing to the increased oxidative damage during ovarian aging.

Increased Apoptosis and Decreased Reductase Activity in Aged Primate Granulosa Cells

We next detected transcriptional noise and identified aging-associated DEGs in somatic cells (Figures 5A and 5B). Most aging-associated changes in gene expression were somatic cell-type-specific (Figure 5B; Table S4), as seen with oocytes. GCs are essential for follicle development and homeostasis as they provide nutrients and mechanical support for oocytes via physical interactions (Rimon-Dahari et al., 2016). As apoptosis of GCs often causes follicular atresia and ovarian aging (Matsuda et al., 2012), we focused on the aging-associated changes of gene expression in GCs. Comparisons between young and aged GCs revealed 62 genes upregulated and 72 downregulated with age (Figure 5B). GO analysis showed that upregulated genes were enriched for "positive regulation of apoptotic process" and downregulated genes were enriched for "oxidoreductase activity" (including *IDH1* [$\log_2$(fold change) = −0.83, p value = 7.8×10^{-5}], *PRDX4* [$\log_2$(fold change) = −0.59, p value = 0.002], and *NDUFB10* [$\log_2$(fold change) = −0.76, p value = 5.4×10^{-5}]) (Figures 5C and 5D; Table S4). Consistently, we also observed increased DNA oxidation (8-OHdG-positive cells) and damage (γH2AX-positive cells) (Figure 5E), along with increased apoptosis (TUNEL-positive cells) and decreased proliferation (Ki67-positive cells) in aged monkey GCs (Figures 5E and 5F) (Khadrawy et al., 2019; Tanabe et al., 2015). The transcriptional regulatory network in GCs showed *ELF4* and *FOSB* as hub genes to regulate the downregulated subset of genes

Figure 4. Downregulation of Antioxidant Genes in Aged Oocytes of Early-Stage Follicles

(A) CV analysis showing the aging-associated transcriptional noise in oocyte subtypes. Left shows the zoom-in view of the region highlighted by a dashed line on the right.

(B) Heatmaps showing the distribution of DEGs between old and young monkeys in each oocyte subtype. The gray bars on the left of the heatmaps denote DEGs shared by at least two oocyte subtypes and the others are oocyte subtype-specific DEGs.

(C) Representative GO terms of downregulated enrichment between old and young monkeys in each oocyte subtype (C1–C3). Top 10 terms for each subtype are listed based on the normalized enrichment score (NES). The nominal p value < 0.05 and false discovery rate (FDR) (q value) < 0.1.

(D) Dot plot showing expression patterns of overlapping genes downregulated in each aged oocyte subtype and included in the GenAge database.

(E) Regulatory network visualizing potential key transcriptional regulators in downregulated DEGs in aged C2 oocytes. Top 5 nodes are colored in light blue and downregulated genes in (D) are in dark blue.

(F) Violin plots showing expression levels of *GPX1* and *GSR* in oocyte subtypes. Two-tailed t test p values are indicated.

(G) Immunofluorescence analysis showing the downregulation of GPX1 and GSR in aged oocytes in primordial and primary follicles in comparison to young counterparts. Scale bar, 50 μm. n = 4 monkeys. *p < 0.05 and **p < 0.01 (two-tailed t test).

See also Figures S4 and S5; Tables S3 and S4.

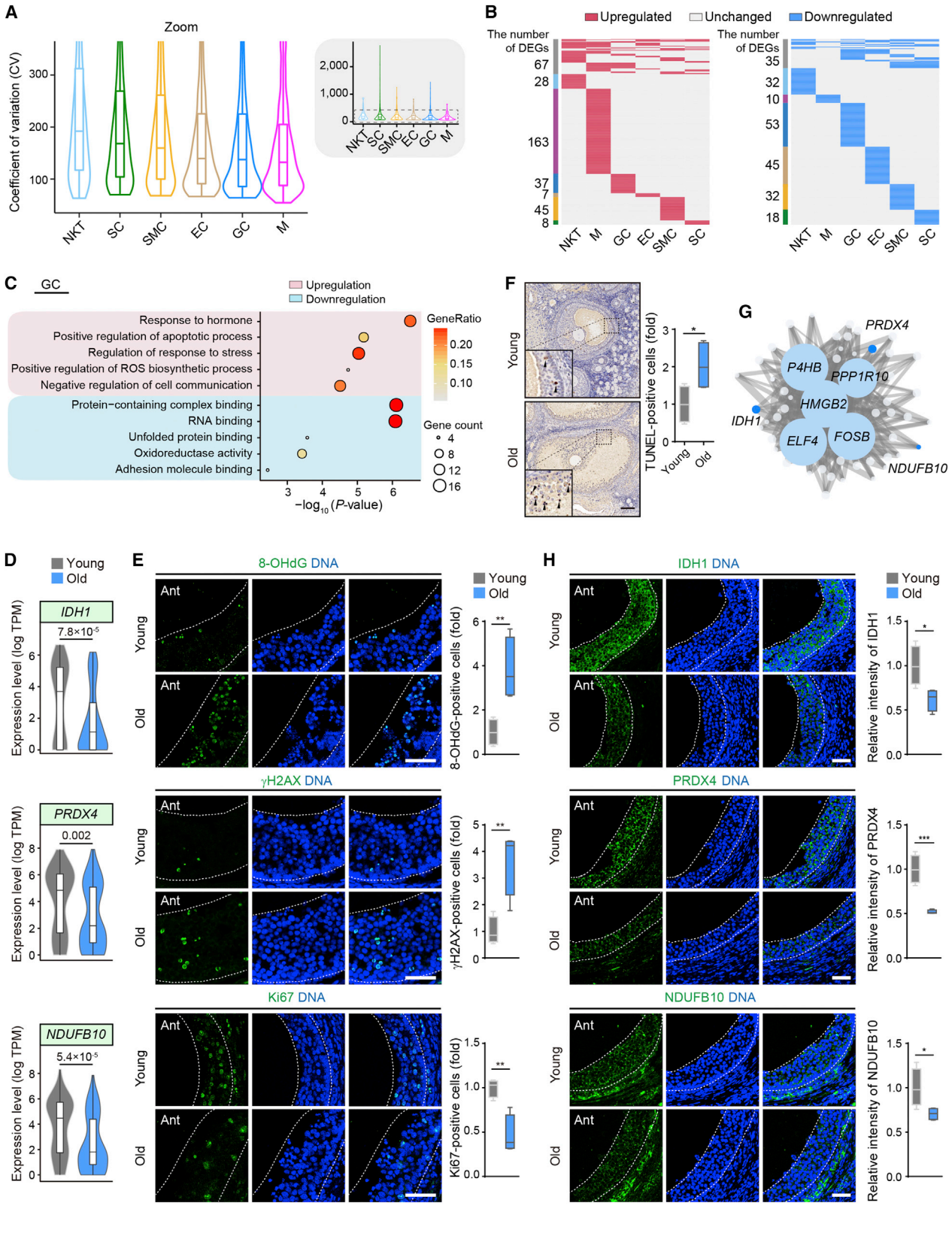

(legend on next page)

(Figures 5G and S6A). Protein levels of these antioxidant genes were also decreased in aged GCs in comparison with GCs from young ovaries (Figure 5H). Altogether, these findings suggest that the downregulation of genes involved in reductase activity could contribute to the compromised antioxidative responses in aged GCs.

Knockdown of Antioxidant Genes in Human Granulosa Cells Recapitulated the Major Phenotypes of Aged Monkey Granulosa Cells

To determine whether these antioxidant genes are also downregulated in human GCs (hGCs) during aging, we obtained hGCs from healthy women from 21 to 46 years old (Figures 6A and S6B). First, we observed aging-associated increased reactive oxygen species (ROS) levels and apoptosis in hGCs from healthy donors, further supporting the aggravated oxidative damage in hGCs during physiological aging (Figure 6B). Consistent with the results in monkeys, hGCs exhibited aging-associated downregulation of *IDH1*, *PRDX4*, and *NDUFB10* (Figure 6C). Next, we explored the effect of silencing these antioxidant genes in a human granulosa cell line (KGN cells) by using small interfering RNAs (siRNAs), with knockdown efficiencies individually validated by RT-qPCR and western blotting (Figures S6C and S6D). Knockdown of *IDH1* and *NDUFB10* decreased cell proliferation (Figure 6D). H_2O_2 treatment further slowed the proliferation of *IDH1*-, *NDUFB10*-, or *PRDX4*-knockdown cells (Figure 6D). In addition, knockdown of *IDH1* or *NDUFB10* resulted in increased mitochondrial mass (Mito-Mass) and mitochondrial depolarization (Figures 6E and 6F), as well as increased cellular ROS levels and apoptosis (Figures 6G and 6H), under oxidative conditions.

Genome-wide RNA-seq analysis (Figures 6I and S6E–S6H; Table S5) further revealed that *IDH1* or *NDUFB10* knockdown upregulated 118 and 156 genes and downregulated 405 and 381 genes, respectively (Figure S6G; Table S5). GO analysis showed that the upregulated genes were enriched in terms "regulation of cell death" and "response to stimulus" upon knockdown of *IDH1*, as well as "positive regulation of cellular senescence" upon knockdown of *NDUFB10*, whereas the downregulated genes were both mainly associated with oxidoreductase activity (Figure 6I; Table S5). We next asked whether these transcriptional changes in human cells were similar to those in monkey GCs during ovarian aging. In the presence of H_2O_2 treatment, five genes were upregulated and seven genes were downregulated both in *IDH1*-knockdown human granulosa cell line and GCs from aged monkeys, whereas six upregulated and 11 downregulated genes were shared by *NDUFB10*-knockdown human granulosa cell line and GCs from aged monkeys (Figure S6I). Notably, several commonly downregulated genes, such as *DCXR* and *TXNIP*, are involved in cellular redox homeostasis (Figure S6I), likely associated to the imbalance of redox homeostasis in aged GCs. Altogether, these results indicate that *IDH1* and *NDUFB10* protect GCs from aging-related oxidative stress in both humans and monkeys (Figure 6J), and the conclusions derived from the scRNA-seq analysis of monkey ovaries are relevant to ovarian aging in humans.

DISCUSSION

Due to the difficulty in obtaining critical human tissues such as ovaries, it has been challenging to determine the molecular mechanisms underlying ovarian aging. In this study, we present the first single-cell survey of ovarian aging in NHPs that show similar genetic and physiological characteristics to humans, providing insights into the mechanisms by which primate ovaries age. These analyses provided four noteworthy contributions. First, we elucidated gene-expression signatures for seven types of primate ovarian cells (including oocyte and ovarian somatic cells) and identified several previously unreported oocyte markers. Second, it allowed for the identification of four NHP oocyte subtypes associated with different stages of folliculogenesis, as well as stage-specific gene regulatory networks. Third, analysis of age-associated gene-expression changes revealed cell-type-specific downregulation of antioxidant genes in aged monkey oocytes and GCs. Fourth, human GCs exhibited similar aging-associated downregulation of antioxidant genes, which was linked to increased oxidative damage. Altogether, these observations provide novel insights into primate ovarian aging and identify new biomarkers and targets for the diagnosis and treatment of human disorders associated with ovarian aging.

Because of limited material availability, few studies concerning the cell compositions of adult and aged ovaries have been reported, particularly for primate ovaries. Han et al. (2018) recently used the Microwell-seq technique to generate a mouse multiple-organ cell atlas that included the ovary. Yet, due to the limited input cell size, their study was restricted to

Figure 5. Downregulation of Genes Involved in Oxidative Stress Response

(A) CV analysis showing the aging-associated transcriptional noise in different ovarian somatic cell types. Left panel shows the zoom-in view of the region highlighted by a dashed line on the right.

(B) Heatmaps showing the distribution of DEGs between old and young monkeys in each somatic cell type. The gray bars on the left of the heatmaps denote DEGs shared by at least two somatic cell types and the others are cell-type-specific DEGs.

(C) Representative GO terms of upregulated (top) or downregulated (bottom) DEGs between old and young monkey granulosa cells (GCs).

(D) Violin plots showing expression levels of *IDH1*, *PRDX4*, and *NDUFB10* in young and old GCs. Two-tailed t test p values are indicated.

(E) Quantification of 8-OHdG-positive (top), γH2AX-positive (middle), and Ki67-positive (bottom) GCs in monkey ovaries. Dashed lines show boundaries of GCs in antral follicles. Ant, antrum. Scale bar, 30 μm. n = 4 monkeys. $^{**}p < 0.01$ (two-tailed t test).

(F) TUNEL staining of young and old GCs. Arrowheads indicate the TUNEL-positive GCs. Scale bar, 100 μm. n = 4 monkeys. $^{*}p < 0.05$ (two-tailed t test).

(G) Regulatory network visualizing potential key transcriptional regulators in downregulated DEGs in aged GCs. Top 5 nodes are colored in light blue and downregulated antioxidant genes are in dark blue.

(H) Immunofluorescence analysis showing the downregulation of *IDH1*, *PRDX4*, and *NDUFB10* in old GCs in comparison to young GCs. Dashed lines show boundaries of GCs in antral follicles. Ant, antrum. Scale bar, 50 μm. n = 4 monkeys. $^{*}p < 0.05$ and $^{***}p < 0.001$ (two-tailed t test).

See also Figure S6 and Table S4.

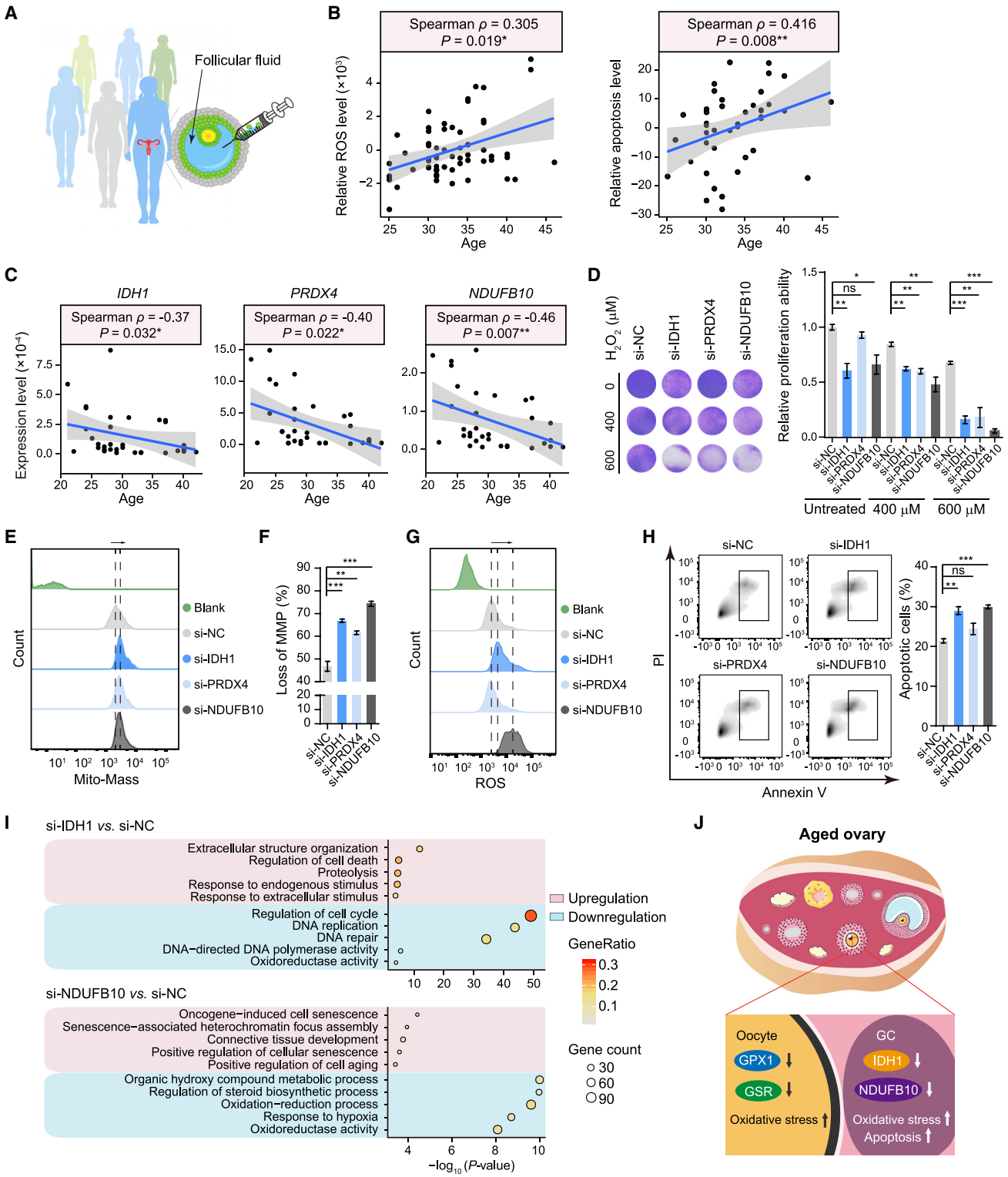

Figure 6. Knockdown of Antioxidant Genes Impaired Proliferation and Redox Homeostasis in Human Granulosa Cells

(A) A schematic showing the procedure for hGC isolation.

(B) The positive correlation of relative ROS levels (left) and apoptosis levels (right) with age in hGCs. The shadow indicates the 0.95 confidence interval around smooth. n = 59 and 43 donors for ROS and apoptosis analyses, respectively.

(legend continued on next page)

ovarian somatic cells, not oocytes. Here, we obtained both oocytes and ovarian somatic cells and successfully mapped the first single-cell transcriptomic atlas of young and aged NHP ovaries by using a modified STRT technique that could detect abundant genes per cell with high efficiency, providing high-quality data to uncover in-depth age-related gene-expression alterations of ovarian cells at single-cell level.

Regarding the cellular composition of the primate ovary, we identified six ovarian somatic compartments and four subtypes of oocytes based on their unique scRNA-seq molecular signatures. The majority of canonical markers were restricted to their specific "island," confirming the robustness of the scRNA-seq strategy and reliability of our data. Although our findings improve the understanding of ovarian cell types in primates, the absence of a cell cluster with lutein cell signature implies that either lutein cells are difficult to obtain or the number of sampled cells was limited by the current method. Therefore, spatiotemporal transcriptomic analysis of other ovarian somatic cell types could be needed in future studies.

Most of the previous studies detailed morphological changes during ovarian aging in primates, but the molecular mechanisms underlying ovarian aging remain largely unknown. A microarray-based gene-expression analysis illustrated the aging-associated molecular alteration in ovaries from rhesus monkeys (Wei et al., 2015). However, due to the heterogeneity of ovarian cell types, the bulk-seq results might not tell whether these changes were intrinsic molecular changes, or simply reflected the changes in the proportions of cell types. By using scRNA-seq (Enge et al., 2017; Kowalczyk et al., 2015; Martinez-Jimenez et al., 2017), we delineate comprehensive cell-type-specific and age-associated gene-expression changes in primate ovaries.

We show that primate ovarian aging is linked to the cell-type-specific downregulation of antioxidant proteins and the upregulation of oxidative damage markers. Supporting these findings, the dysregulation of antioxidant system has been reported in many aging-related contexts (Agarwal et al., 2005; Kubben et al., 2016). Consistently, bulk RNA-seq has revealed age-related mitochondrial dysfunction and oxidative damage in mouse ovarian somatic cells and MII oocyte populations collected from women undergoing assisted reproductive technology (ART) (Grøndahl et al., 2010; Lim and Luderer, 2011; Steuerwald et al., 2007). Through scRNA-seq analysis, our study shows that in monkeys, the inactivation of the antioxidative system occurs in both aged oocytes and aged GCs by different regulatory mechanisms, evidenced by the cell-type-specific transcriptional regulatory networks involving distinct hub genes in oocytes and niche cells. Moreover, our single-cell transcriptomic atlas of primate ovarian aging was mapped on samples collected from monkey ovaries with a wider age range than female donors undergoing ART and also included oocytes from almost all follicle stages, which undoubtedly provides invaluable in-depth information to ovarian aging biology. Furthermore, the expression levels of antioxidant genes were negatively correlated with age in human GCs, and *IDH1* or *NDUFB10* knockdown impaired oxidative stress responses, highlighting these genes as biomarkers and targets for diagnosing and treating human age-related ovarian diseases and for female fertility preservation.

In summary, this study provides the first comprehensive single-cell transcriptomic atlas of ovaries of young and aged NHPs and broadens our understanding of cell identities and cell-type-specific gene signatures in the primate ovary. Importantly, it offers insights of the molecular mechanisms underlying ovarian aging in humans and lays a foundation for the quantitative assessment of oocyte quality and reproductive age of human. Moreover, great efforts are being invested for the generation of gametes and ovarian cell types from pluripotent stem cells. The single-cell transcriptomic atlas from young and aged ovaries presented here can be a great resource and platform to determine the quality and capacity of differentiated gametes in maintaining distinct gene-expression signatures, as well as to facilitate optimizing conditions toward obtaining superior quality gametes. In addition, the mechanistic insights arising from this study could establish new avenues for developing targeted antioxidant interventions to protect against physiological ovarian aging and related diseases and for developing new tools for aged oocyte rejuvenation for assisted reproductive therapies and female fertility preservation.

STAR★METHODS

Detailed methods are provided in the online version of this paper and include the following:

- KEY RESOURCES TABLE
- LEAD CONTACT AND MATERIALS AVAILABILITY

(C) The negative correlation of mRNA levels of *IDH1*, *PRDX4*, and *NDUFB10* with age in hGCs. 18S rRNA was used as loading control to normalize mRNA levels. The shadow indicates the 0.95 confidence interval around smooth. n = 33 donors.
(D) Proliferation ability of KGN cells upon *IDH1*, *PRDX4*, or *NDUFB10* knockdown with or without H_2O_2 treatment. Data are shown as the mean ± SEM, n = 3, ns, not significant, *p < 0.05, **p < 0.01 and ***p < 0.001 (two-tailed t test).
(E) Mitochondrial mass in *IDH1*-, *PRDX4*-, or *NDUFB10*-knockdown KGN cells upon H_2O_2 treatment assessed by NAO signal intensity.
(F) Loss of mitochondrial membrane potential (MMP) in *IDH1*-, *PRDX4*-, or *NDUFB10*-knockdown KGN cells upon H_2O_2 treatment assessed by the percentage of cells with JC-10 monomer by flow cytometry. Data are presented as the mean ± SEM, n = 3, **p < 0.01 and ***p < 0.001 (two-tailed t test).
(G) Cellular ROS levels in *IDH1*-, *PRDX4*-, or *NDUFB10*-knockdown KGN cells upon H_2O_2 treatment.
(H) Apoptosis of *IDH1*-, *PRDX4*-, or *NDUFB10*-knockdown KGN cells upon H_2O_2 treatment. Quantitative data are shown as the mean ± SEM to the right, n = 3, ns, not significant, **p < 0.01 and ***p < 0.001 (two-tailed t test).
(I) Representative GO terms of DEGs in *IDH1*- (top) or *NDUFB10*-knockdown cells (bottom) in comparison to negative controls. DEGs were identified by $|\log_2$ (fold change)$| \geq 1$ and both the p value and FDR were <0.05.
(J) A schematic illustration showing cell-type-specific downregulation of genes involved in redox homeostasis maintenance in aged primate oocytes and GCs, which could contribute to increased oxidative damage and cell apoptosis.
See also Figure S6; Table S5.

SUPPLEMENTAL INFORMATION

Supplemental Information can be found online at https://doi.org/10.1016/j.cell.2020.01.009.

ACKNOWLEDGMENTS

The authors acknowledge L. Bai, R. Bai, Q. Chu, J. Lu, S. Ma, and Y. Yang for administrative assistance; H. Wan, W. Li, X. Ma, C. Ling, and the Liu lab members for their help in animal experiments and insightful opinions; and J. Jia (IBP, CAS) and S. Sun (IBP, CAS) for their help in the FACS experiments. Part of the bioinformatics analysis was performed on the computing platform of the Center for Life Science. This work was supported by the National Key Research and Development Program of China (2018YFC2000100), the Strategic Priority Research Program of the Chinese Academy of Sciences (XDA16010100), the National Key Research and Development Program of China (2017YFA0102802, 2017YFA0103304, 2018YFC1003101, 2015CB964800, 2016YFC1000601, 2018YFA0107203, 2018YFC2000400), the National Natural Science Foundation of China (81921006, 81625009, 91749202, 91749123, 31671429, 81671377, 81771515, 31601158, 81701388, 81601233, 31601109, 81822018, 81870228, 81801399, 31801010, 81801370, 81861168034, 31900523, 81901432, 81901433, 31900524, 81922027, 81571400, 81771580, 81971381, 81730038, 81571385, 91849132, 91949209), Beijing Natural Science Foundation (Z190019), Program of Beijing Municipal Science and Technology Commission (Z191100001519005), Beijing Municipal Commission of Health and Family Planning (PXM2018_026283_000002), the Key Research Program of the Chinese Academy of Sciences (KFZD-SW-221), Advanced Innovation Center for Human Brain Protection (3500-1192012), Young Elite Scientists Sponsorship Program by CAST (2017QNRC001), the State Key Laboratory of Membrane Biology, and the Strategic Collaborative Research Program of the Ferring Institute of Reproductive Medicine, Ferring Pharmaceuticals and the Chinese Academy of Sciences (FIRMC180305). J.C.I.B. was supported by UCAM, the Moxie Foundation, and the Glenn Foundation.

AUTHOR CONTRIBUTIONS

G.-H.L., F.T., J. Qu, and J.C.I.B. conceptualized this project and supervised the overall experiments. S.W. and J.L. performed isolation of ovarian cells and scRNA-seq library construction and sequencing. Y.Z. performed bioinformatics analysis of the scRNA-seq and bulk RNA-seq data. S.W., W.Z., and H.H. performed ovary histological analysis. S.W., Y.Y., Z.M., Y.J., and L.M. performed cell culture as well as functional and mechanistic analyses. G.-H.L., F.T., J. Qu, J.C.I.B., S.W., Y.Z., M.S., J.L., W.Z., Z.L., X.H., C.R.E., L.S., P.C., J. Qiao, and Q.Z. performed manuscript writing, review, and editing.

DECLARATION OF INTERESTS

The authors declare no competing interests.

Received: June 4, 2019
Revised: September 13, 2019
Accepted: January 6, 2020
Published: January 30, 2020

REFERENCES

Agarwal, A., Gupta, S., and Sharma, R.K. (2005). Role of oxidative stress in female reproduction. Reprod. Biol. Endocrinol. *3*, 28.

Aibar, S., González-Blas, C.B., Moerman, T., Huynh-Thu, V.A., Imrichova, H., Hulselmans, G., Rambow, F., Marine, J.C., Geurts, P., Aerts, J., et al. (2017). SCENIC: single-cell regulatory network inference and clustering. Nat. Methods *14*, 1083–1086.

Anders, S., Pyl, P.T., and Huber, W. (2015). HTSeq–a Python framework to work with high-throughput sequencing data. Bioinformatics *31*, 166–169.

Anderson, R.M., and Colman, R.J. (2011). Prospects and perspectives in primate aging research. Antioxid. Redox Signal. *14*, 203–205.

Appt, S.E., Chen, H., Goode, A.K., Hoyer, P.B., Clarkson, T.B., Adams, M.R., Wilson, M.E., Franke, A.A., and Kaplan, J.R. (2010). The effect of diet and cardiovascular risk on ovarian aging in cynomolgus monkeys (Macaca fascicularis). Menopause *17*, 741–748.

Atkins, H.M., Willson, C.J., Silverstein, M., Jorgensen, M., Floyd, E., Kaplan, J.R., and Appt, S.E. (2014). Characterization of ovarian aging and reproductive senescence in vervet monkeys (Chlorocebus aethiops sabaeus). Comp. Med. *64*, 55–62.

Baryawno, N., Przybylski, D., Kowalczyk, M.S., Kfoury, Y., Severe, N., Gustafsson, K., Kokkaliaris, K.D., Mercier, F., Tabaka, M., Hofree, M., et al. (2019). A Cellular Taxonomy of the Bone Marrow Stroma in Homeostasis and Leukemia. Cell *177*, 1915–1932.

Bellino, F.L., and Wise, P.M. (2003). Nonhuman primate models of menopause workshop. Biol. Reprod. *68*, 10–18.

Broekmans, F.J., Soules, M.R., and Fauser, B.C. (2009). Ovarian aging: mechanisms and clinical consequences. Endocr. Rev. *30*, 465–493.

Buck, T., Hack, C.T., Berg, D., Berg, U., Kunz, L., and Mayerhofer, A. (2019). The NADPH oxidase 4 is a major source of hydrogen peroxide in human granulosa-lutein and granulosa tumor cells. Sci. Rep. *9*, 3585.

Bult, C.J., Blake, J.A., Smith, C.L., Kadin, J.A., and Richardson, J.E.; Mouse Genome Database Group (2019). Mouse Genome Database (MGD) 2019. Nucleic Acids Res. *47* (D1), D801–D806.

Cao, J., Spielmann, M., Qiu, X., Huang, X., Ibrahim, D.M., Hill, A.J., Zhang, F., Mundlos, S., Christiansen, L., Steemers, F.J., et al. (2019). The single-cell transcriptional landscape of mammalian organogenesis. Nature *566*, 496–502.

Castrillon, D.H., Quade, B.J., Wang, T.Y., Quigley, C., and Crum, C.P. (2000). The human VASA gene is specifically expressed in the germ cell lineage. Proc. Natl. Acad. Sci. USA *97*, 9585–9590.

Chen, J., Bardes, E.E., Aronow, B.J., and Jegga, A.G. (2009). ToppGene Suite for gene list enrichment analysis and candidate gene prioritization. Nucleic Acids Res. *37*, W305-11.

Cheng, F., Wang, S., Song, M., Liu, Z., Liu, P., Wang, L., Wang, Y., Zhao, Q., Yan, K., Chan, P., et al. (2019). DJ-1 is dispensable for human stem cell homeostasis. Protein Cell *10*, 846–853.

Colman, R.J. (2018). Non-human primates as a model for aging. Biochim. Biophys. Acta Mol. Basis Dis. *1864* (9 Pt A), 2733–2741.

Cordts, E.B., Christofolini, D.M., Dos Santos, A.A., Bianco, B., and Barbosa, C.P. (2011). Genetic aspects of premature ovarian failure: a literature review. Arch. Gynecol. Obstet. *283*, 635–643.

Cui, Y., Zheng, Y., Liu, X., Yan, L., Fan, X., Yong, J., Hu, Y., Dong, J., Li, Q., Wu, X., et al. (2019). Single-cell transcriptome analysis maps the developmental track of the human heart. Cell Rep. *26*, 1934–1950.e5.

Davie, K., Janssens, J., Koldere, D., De Waegeneer, M., Pech, U., Kreft, L., Aibar, S., Makhzami, S., Christiaens, V., Bravo Gonzalez-Blas, C., et al. (2018). A Single-Cell Transcriptome Atlas of the Aging Drosophila Brain. Cell *174*, 982–998.

de Magalhães, J.P., Budovsky, A., Lehmann, G., Costa, J., Li, Y., Fraifeld, V., and Church, G.M. (2009). The Human Ageing Genomic Resources: online databases and tools for biogerontologists. Aging Cell *8*, 65–72.

Dong, J., Albertini, D.F., Nishimori, K., Kumar, T.R., Lu, N., and Matzuk, M.M. (1996). Growth differentiation factor-9 is required during early ovarian folliculogenesis. Nature *383*, 531–535.

Dong, J., Hu, Y., Fan, X., Wu, X., Mao, Y., Hu, B., Guo, H., Wen, L., and Tang, F. (2018). Single-cell RNA-seq analysis unveils a prevalent epithelial/mesenchymal hybrid state during mouse organogenesis. Genome Biol. *19*, 31.

Drevon-Gaillot, E., Perron-Lepage, M.F., Clément, C., and Burnett, R. (2006). A review of background findings in cynomolgus monkeys (Macaca fascicularis) from three different geographical origins. Exp. Toxicol. Pathol. *58*, 77–88.

Enge, M., Arda, H.E., Mignardi, M., Beausang, J., Bottino, R., Kim, S.K., and Quake, S.R. (2017). Single-Cell Analysis of Human Pancreas Reveals Transcriptional Signatures of Aging and Somatic Mutation Patterns. Cell *171*, 321–330.

Ferrero, H., Delgado-Rosas, F., Garcia-Pascual, C.M., Monterde, M., Zimmermann, R.C., Simón, C., Pellicer, A., and Gómez, R. (2012). Efficiency and purity provided by the existing methods for the isolation of luteinized granulosa cells: a comparative study. Hum. Reprod. *27*, 1781–1789.

Feuerstein, P., Cadoret, V., Dalbies-Tran, R., Guerif, F., Bidault, R., and Royere, D. (2007). Gene expression in human cumulus cells: one approach to oocyte competence. Hum. Reprod. *22*, 3069–3077.

Gao, S., Yan, L., Wang, R., Li, J., Yong, J., Zhou, X., Wei, Y., Wu, X., Wang, X., Fan, X., et al. (2018). Publisher Correction: Tracing the temporal-spatial transcriptome landscapes of the human fetal digestive tract using single-cell RNA-sequencing. Nat. Cell Biol. *20*, 1227.

Gerstberger, S., Meyer, C., Benjamin-Hong, S., Rodriguez, J., Briskin, D., Bognanni, C., Bogardus, K., Steller, H., and Tuschl, T. (2017). The conserved RNA exonuclease Rexo5 is required for 3′ end maturation of 28S rRNA, 5S rRNA, and snoRNAs. Cell Rep. *21*, 758–772.

Grøndahl, M.L., Yding Andersen, C., Bogstad, J., Nielsen, F.C., Meinertz, H., and Borup, R. (2010). Gene expression profiles of single human mature oocytes in relation to age. Hum. Reprod. *25*, 957–968.

Gu, C., Liu, S., Wu, Q., Zhang, L., and Guo, F. (2019). Integrative single-cell analysis of transcriptome, DNA methylome and chromatin accessibility in mouse oocytes. Cell Res. *29*, 110–123.

Haghverdi, L., Lun, A.T.L., Morgan, M.D., and Marioni, J.C. (2018). Batch effects in single-cell RNA-sequencing data are corrected by matching mutual nearest neighbors. Nat. Biotechnol. *36*, 421–427.

Han, X., Wang, R., Zhou, Y., Fei, L., Sun, H., Lai, S., Saadatpour, A., Zhou, Z., Chen, H., Ye, F., et al. (2018). Mapping the Mouse Cell Atlas by Microwell-Seq. Cell *172*, 1091–1107.

Harris, M.A., Clark, J., Ireland, A., Lomax, J., Ashburner, M., Foulger, R., Eilbeck, K., Lewis, S., Marshall, B., Mungall, C., et al.; Gene Ontology Consortium (2004). The Gene Ontology (GO) database and informatics resource. Nucleic Acids Res. *32*, D258–D261.

Hatzirodos, N., Hummitzsch, K., Irving-Rodgers, H.F., and Rodgers, R.J. (2015). Transcriptome comparisons identify new cell markers for theca interna and granulosa cells from small and large antral ovarian follicles. PLoS ONE *10*, e0119800.

Hochgerner, H., Lönnerberg, P., Hodge, R., Mikes, J., Heskol, A., Hubschle, H., Lin, P., Picelli, S., La Manno, G., Ratz, M., et al. (2017). STRT-seq-2i: dual-index 5′ single cell and nucleus RNA-seq on an addressable microwell array. Sci. Rep. *7*, 16327.

Hu, K.L., Zhao, H., Min, Z., He, Y., Li, T., Zhen, X., Ren, Y., Chang, H.M., Yu, Y., and Li, R. (2019). Increased expression of KISS1 and KISS1 receptor in human granulosa lutein cells-potential pathogenesis of polycystic ovary syndrome. Reprod. Sci. *26*, 1429–1438.

Huynh-Thu, V.A., Irrthum, A., Wehenkel, L., and Geurts, P. (2010). Inferring regulatory networks from expression data using tree-based methods. PLoS ONE *5*, e12776.

Islam, S., Kjällquist, U., Moliner, A., Zajac, P., Fan, J.B., Lönnerberg, P., and Linnarsson, S. (2011). Characterization of the single-cell transcriptional landscape by highly multiplex RNA-seq. Genome Res. *21*, 1160–1167.

Johnson, J., Canning, J., Kaneko, T., Pru, J.K., and Tilly, J.L. (2004). Germline stem cells and follicular renewal in the postnatal mammalian ovary. Nature *428*, 145–150.

Kavanagh, K., Koudy Williams, J., and Wagner, J.D. (2005). Naturally occurring menopause in cynomolgus monkeys: changes in hormone, lipid, and carbohydrate measures with hormonal status. J. Med. Primatol. *34*, 171–177.

Khadrawy, O., Gebremedhn, S., Salilew-Wondim, D., Taqi, M.O., Neuhoff, C., Tholen, E., Hoelker, M., Schellander, K., and Tesfaye, D. (2019). Endogenous and Exogenous Modulation of Nrf2 Mediated Oxidative Stress Response in Bovine Granulosa Cells: Potential Implication for Ovarian Function. Int. J. Mol. Sci. *20*, E1635.

Kowalczyk, M.S., Tirosh, I., Heckl, D., Rao, T.N., Dixit, A., Haas, B.J., Schneider, R.K., Wagers, A.J., Ebert, B.L., and Regev, A. (2015). Single-cell RNA-seq reveals changes in cell cycle and differentiation programs upon aging of hematopoietic stem cells. Genome Res. *25*, 1860–1872.

Kubben, N., Zhang, W., Wang, L., Voss, T.C., Yang, J., Qu, J., Liu, G.H., and Misteli, T. (2016). Repression of the Antioxidant NRF2 Pathway in Premature Aging. Cell *165*, 1361–1374.

Kurioka, A., Cosgrove, C., Simoni, Y., van Wilgenburg, B., Geremia, A., Björkander, S., Sverremark-Ekström, E., Thurnheer, C., Günthard, H.F., Khanna, N., et al.; Swiss HIV Cohort Study; Oxford IBD Cohort Investigators (2018). CD161 Defines a Functionally Distinct Subset of Pro-Inflammatory Natural Killer Cells. Front. Immunol. *9*, 486.

Lake, B.B., Ai, R., Kaeser, G.E., Salathia, N.S., Yung, Y.C., Liu, R., Wildberg, A., Gao, D., Fung, H.L., Chen, S., et al. (2016). Neuronal subtypes and diversity revealed by single-nucleus RNA sequencing of the human brain. Science *352*, 1586–1590.

Lass, A., Silye, R., Abrams, D.C., Krausz, T., Hovatta, O., Margara, R., and Winston, R.M. (1997). Follicular density in ovarian biopsy of infertile women: a novel method to assess ovarian reserve. Hum. Reprod. *12*, 1028–1031.

Li, Q., Geng, X., Zheng, W., Tang, J., Xu, B., and Shi, Q. (2012). Current understanding of ovarian aging. Sci. China Life Sci. *55*, 659–669.

Lim, J., and Luderer, U. (2011). Oxidative damage increases and antioxidant gene expression decreases with aging in the mouse ovary. Biol. Reprod. *84*, 775–782.

Lim, J., Lee, M., Son, A., Chang, H., and Kim, V.N. (2016). mTAIL-seq reveals dynamic poly(A) tail regulation in oocyte-to-embryo development. Genes Dev. *30*, 1671–1682.

Ling, C., Liu, Z., Song, M., Zhang, W., Wang, S., Liu, X., Ma, S., Sun, S., Fu, L., Chu, Q., et al. (2019). Modeling CADASIL vascular pathologies with patient-derived induced pluripotent stem cells. Protein Cell *10*, 249–271.

Liu, X., Wang, W., Samarsky, D., Liu, L., Xu, Q., Zhang, W., Zhu, G., Wu, P., Zuo, X., Deng, H., et al. (2014). Tumor-targeted *in vivo* gene silencing via systemic delivery of cRGD-conjugated siRNA. Nucleic Acids Res. *42*, 11805–11817.

Love, M.I., Huber, W., and Anders, S. (2014). Moderated estimation of fold change and dispersion for RNA-seq data with DESeq2. Genome Biol. *15*, 550.

Lun, A.T., McCarthy, D.J., and Marioni, J.C. (2016). A step-by-step workflow for low-level analysis of single-cell RNA-seq data with Bioconductor. F1000Res. *5*, 2122.

Magoffin, D.A. (2005). Ovarian theca cell. Int. J. Biochem. Cell Biol. *37*, 1344–1349.

Markholt, S., Grøndahl, M.L., Ernst, E.H., Andersen, C.Y., Ernst, E., and Lykke-Hartmann, K. (2012). Global gene analysis of oocytes from early stages in human folliculogenesis shows high expression of novel genes in reproduction. Mol. Hum. Reprod. *18*, 96–110.

Martinez-Jimenez, C.P., Eling, N., Chen, H.C., Vallejos, C.A., Kolodziejczyk, A.A., Connor, F., Stojic, L., Rayner, T.F., Stubbington, M.J.T., Teichmann, S.A., et al. (2017). Aging increases cell-to-cell transcriptional variability upon immune stimulation. Science *355*, 1433–1436.

Matsuda, F., Inoue, N., Manabe, N., and Ohkura, S. (2012). Follicular growth and atresia in mammalian ovaries: regulation by survival and death of granulosa cells. J. Reprod. Dev. *58*, 44–50.

Meinsohn, M.C., Morin, F., Bertolin, K., Duggavathi, R., Schoonjans, K., and Murphy, B.D. (2017). The orphan nuclear receptor liver homolog receptor-1 (Nr5a2) regulates ovarian granulosa cell proliferation. J. Endocr. Soc. *2*, 24–41.

Morita, Y., Perez, G.I., Maravei, D.V., Tilly, K.I., and Tilly, J.L. (1999). Targeted expression of Bcl-2 in mouse oocytes inhibits ovarian follicle atresia and prevents spontaneous and chemotherapy-induced oocyte apoptosis in vitro. Mol. Endocrinol. *13*, 841–850.

Nichols, S.M., Bavister, B.D., Brenner, C.A., Didier, P.J., Harrison, R.M., and Kubisch, H.M. (2005). Ovarian senescence in the rhesus monkey (*Macaca mulatta*). Hum. Reprod. *20*, 79–83.

Nicosia, S.V. (1987). The aging ovary. Med. Clin. North Am. *71*, 1–9.

Nishi, Y., Yanase, T., Mu, Y., Oba, K., Ichino, I., Saito, M., Nomura, M., Mukasa, C., Okabe, T., Goto, K., et al. (2001). Establishment and characterization of a steroidogenic human granulosa-like tumor cell line, KGN, that expresses functional follicle-stimulating hormone receptor. Endocrinology *142*, 437–445.

Owens, G.K., Kumar, M.S., and Wamhoff, B.R. (2004). Molecular regulation of vascular smooth muscle cell differentiation in development and disease. Physiol. Rev. *84*, 767–801.

Perheentupa, A., and Huhtaniemi, I. (2009). Aging of the human ovary and testis. Mol. Cell. Endocrinol. *299*, 2–13.

Perry, J.R., Murray, A., Day, F.R., and Ong, K.K. (2015). Molecular insights into the aetiology of female reproductive ageing. Nat. Rev. Endocrinol. *11*, 725–734.

Prieto, I., Tease, C., Pezzi, N., Buesa, J.M., Ortega, S., Kremer, L., Martínez, A., Martínez-A, C., Hultén, M.A., and Barbero, J.L. (2004). Cohesin component dynamics during meiotic prophase I in mammalian oocytes. Chromosome Res. *12*, 197–213.

Randi, A.M., Smith, K.E., and Castaman, G. (2018). von Willebrand factor regulation of blood vessel formation. Blood *132*, 132–140.

Rimon-Dahari, N., Yerushalmi-Heinemann, L., Alyagor, L., and Dekel, N. (2016). Ovarian Folliculogenesis. Results Probl. Cell Differ. *58*, 167–190.

Ringuette, M.J., Sobieski, D.A., Chamow, S.M., and Dean, J. (1986). Oocyte-specific gene expression: molecular characterization of a cDNA coding for ZP-3, the sperm receptor of the mouse zona pellucida. Proc. Natl. Acad. Sci. USA *83*, 4341–4345.

Rossetti, R., Ferrari, I., Bonomi, M., and Persani, L. (2017). Genetics of primary ovarian insufficiency. Clin. Genet. *91*, 183–198.

Salzer, M.C., Lafzi, A., Berenguer-Llergo, A., Youssif, C., Castellanos, A., Solanas, G., Peixoto, F.O., Stephan-Otto Attolini, C., Prats, N., Aguilera, M., et al. (2018). Identity Noise and Adipogenic Traits Characterize Dermal Fibroblast Aging. Cell *175*, 1575–1590.

Sánchez, F., and Smitz, J. (2012). Molecular control of oogenesis. Biochim. Biophys. Acta *1822*, 1896–1912.

Satija, R., Farrell, J.A., Gennert, D., Schier, A.F., and Regev, A. (2015). Spatial reconstruction of single-cell gene expression data. Nat. Biotechnol. *33*, 495–502.

Sha, Q.Q., Zhang, J., and Fan, H.Y. (2019). A story of birth and death: mRNA translation and clearance at the onset of maternal-to-zygotic transition in mammals. Biol. Reprod. *101*, 579–590.

Sousa, S., Brion, R., Lintunen, M., Kronqvist, P., Sandholm, J., Mönkkönen, J., Kellokumpu-Lehtinen, P.L., Lauttia, S., Tynninen, O., Joensuu, H., et al. (2015). Human breast cancer cells educate macrophages toward the M2 activation status. Breast Cancer Res. *17*, 101.

Soyal, S.M., Amleh, A., and Dean, J. (2000). FIGalpha, a germ cell-specific transcription factor required for ovarian follicle formation. Development *127*, 4645–4654.

Steuerwald, N.M., Bermúdez, M.G., Wells, D., Munné, S., and Cohen, J. (2007). Maternal age-related differential global expression profiles observed in human oocytes. Reprod. Biomed. Online *14*, 700–708.

Stevant, I., Kuhne, F., Greenfield, A., Chaboissier, M.C., Dermitzakis, E.T., and Nef, S. (2019). Dissecting Cell Lineage Specification and Sex Fate Determination in Gonadal Somatic Cells Using Single-Cell Transcriptomics. Cell Rep. *26*, 3272–3283.

Stocco, C. (2008). Aromatase expression in the ovary: hormonal and molecular regulation. Steroids *73*, 473–487.

Su, T., Stanley, G., Sinha, R., D'Amato, G., Das, S., Rhee, S., Chang, A.H., Poduri, A., Raftrey, B., Dinh, T.T., et al. (2018). Single-cell analysis of early progenitor cells that build coronary arteries. Nature *559*, 356–362.

Subramanian, A., Tamayo, P., Mootha, V.K., Mukherjee, S., Ebert, B.L., Gillette, M.A., Paulovich, A., Pomeroy, S.L., Golub, T.R., Lander, E.S., and Mesirov, J.P. (2005). Gene set enrichment analysis: a knowledge-based approach for interpreting genome-wide expression profiles. Proc. Natl. Acad. Sci. USA *102*, 15545–15550.

Subtelny, A.O., Eichhorn, S.W., Chen, G.R., Sive, H., and Bartel, D.P. (2014). Poly(A)-tail profiling reveals an embryonic switch in translational control. Nature *508*, 66–71.

Tanabe, M., Tamura, H., Taketani, T., Okada, M., Lee, L., Tamura, I., Maekawa, R., Asada, H., Yamagata, Y., and Sugino, N. (2015). Melatonin protects the integrity of granulosa cells by reducing oxidative stress in nuclei, mitochondria, and plasma membranes in mice. J. Reprod. Dev. *61*, 35–41.

Tilly, J.L., and Sinclair, D.A. (2013). Germline energetics, aging, and female infertility. Cell Metab. *17*, 838–850.

Trapnell, C., Pachter, L., and Salzberg, S.L. (2009). TopHat: discovering splice junctions with RNA-Seq. Bioinformatics *25*, 1105–1111.

Walker, M.L., and Herndon, J.G. (2008). Menopause in nonhuman primates? Biol. Reprod. *79*, 398–406.

Walker, M.L., Anderson, D.C., Herndon, J.G., and Walker, L.C. (2009). Ovarian aging in squirrel monkeys (*Saimiri sciureus*). Reproduction *138*, 793–799.

Wang, S., Wang, X., Wu, Y., and Han, C. (2015). IGF-1R signaling is essential for the proliferation of cultured mouse spermatogonial stem cells by promoting the G2/M progression of the cell cycle. Stem Cells Dev. *24*, 471–483.

Wang, S., Wang, X., Ma, L., Lin, X., Zhang, D., Li, Z., Wu, Y., Zheng, C., Feng, X., Liao, S., et al. (2016). Retinoic acid is sufficient for the *in vitro* induction of mouse spermatocytes. Stem Cell Reports *7*, 80–94.

Wang, S., Hu, B., Ding, Z., Dang, Y., Wu, J., Li, D., Liu, X., Xiao, B., Zhang, W., Ren, R., et al. (2018). ATF6 safeguards organelle homeostasis and cellular aging in human mesenchymal stem cells. Cell Discov. *4*, 2.

Wang, S., Min, Z., Ji, Q., Geng, L., Su, Y., Liu, Z., Hu, H., Wang, L., Zhang, W., Suzuiki, K., et al. (2019). Rescue of premature aging defects in Cockayne syndrome stem cells by CRISPR/Cas9-mediated gene correction. Protein Cell. Published online April 30, 2019. https://doi.org/10.1007/s13238-019-0623-2.

Webb, P.M., and Jordan, S.J. (2017). Epidemiology of epithelial ovarian cancer. Best Pract. Res. Clin. Obstet. Gynaecol. *41*, 3–14.

Wei, H., Liu, X., Yuan, J., Li, L., Zhang, D., Guo, X., Liu, L., and Zhang, S. (2015). Age-specific gene expression profiles of rhesus monkey ovaries detected by microarray analysis. BioMed Res. Int. *2015*, 625192.

Zhang, W., Wan, H., Feng, G., Qu, J., Wang, J., Jing, Y., Ren, R., Liu, Z., Zhang, L., Chen, Z., et al. (2018a). SIRT6 deficiency results in developmental retardation in cynomolgus monkeys. Nature *560*, 661–665.

Zhang, Y., Yan, Z., Qin, Q., Nisenblat, V., Chang, H.M., Yu, Y., Wang, T., Lu, C., Yang, M., Yang, S., et al. (2018b). Transcriptome Landscape of Human Folliculogenesis Reveals Oocyte and Granulosa Cell Interactions. Mol. Cell *72*, 1021–1034.

Zhang, X., Liu, Z., Liu, X., Wang, S., Zhang, Y., He, X., Sun, S., Ma, S., Shyh-Chang, N., Liu, F., et al. (2019). Telomere-dependent and telomere-independent roles of RAP1 in regulating human stem cell homeostasis. Protein Cell *10*, 649–667.

STAR★METHODS

KEY RESOURCES TABLE

REAGENT or RESOURCE	SOURCE	IDENTIFIER
Antibodies		
Rabbit anti-SCP3 (SYCP3)	Abcam	Cat# ab15093; RRID: AB_301639
Rabbit anti-Leiomodin-3 (LMOD3)	Abcam	Cat# ab122305; RRID: AB_11128719
Rabbit anti-RBM46	Thermo Fisher Scientific	Cat# PA5-69118; RRID: AB_2688611
Sheep anti-NETO1	R&D	Cat# AF4337; RRID: AB_2148942
Rabbit anti-LOC81691 (REXO5)	Thermo Fisher Scientific	Cat# PA5-59283; RRID: AB_2643420
Rabbit anti-DDX4 / MVH	Abcam	Cat# ab13840; RRID: AB_443012
Rabbit anti-WT1	Abcam	Cat# ab89901; RRID: AB_2043201
Rabbit anti-AMH	Abgent	Cat# AP9940C; RRID: AB_10663722
Rabbit anti-STAR	Santa Cruz Biotechnology	Cat# sc-25806; RRID: AB_2115937
Mouse anti-SMA	Zsbio, China	Cat# ZM-0003
Rabbit anti-VWF	Dako	Cat# A0082; RRID: AB_2315602
Rabbit anti-DESMIN	Cell Signaling Technology	Cat# 5332; RRID: AB_1903947
Rabbit anti-GPX1	Thermo Fisher Scientific	Cat# PA5-30593; RRID: AB_2548067
Rabbit anti-GSR	Thermo Fisher Scientific	Cat# PA5-79334; RRID: AB_2746450
Rabbit anti-IDH1	Thermo Fisher Scientific	Cat# PA5-28206; RRID: AB_2545682
Rabbit anti-PRDX4	Abcam	Cat# ab184167
Mouse anti-NDUFB10	Thermo Fisher Scientific	Cat# MA5-26082; RRID: AB_2724811
Rabbit anti-TOM20	Santa Cruz Biotechnology	Cat# sc-11415; RRID: AB_2207533
Rabbit anti-ND1	Proteintech Group, Inc	Cat# 19703-1-AP; RRID: AB_10637853
Mouse anti-8-OHdG	Santa Cruz Biotechnology	Cat# sc-66036; RRID: AB_832272
Rabbit anti-Histone H2A.X, phospho (Ser139) (γH2AX)	Cell Signaling Technology	Cat# 9718S; RRID: AB_2118009
Mouse anti-Ki67	Zsbio, China	Cat# ZM-0166
Biological Samples		
Human follicular fluid	Peking University Third Hospital in Beijing	N/A
Cynomolgus monkey ovary tissue	Xieerxin Biology Resource in Beijing	N/A
Chemicals, Peptides, and Recombinant Proteins		
Lipofectamine 3000 Transfection Reagent	Thermo Fisher Scientific	Cat# L3000015
DMEM/F-12 Medium	Thermo Fisher Scientific	Cat# 11330032
FBS	GIBCO	Cat# 10270-106; LOT# 42F9083K
M2 medium	Sigma	Cat# M7167
Collagenase, Type IV	GIBCO	Cat# 17104-019
Trypsin-EDTA (0.25%)	GIBCO	Cat# 25200-072
Hyaluronidase	Sigma	Cat# H-4272
Hydrogen peroxide solution	Sigma	Cat# 323381
Crystal violet	Biohao Biotechnology Co.,Ltd, China	Cat# C0502
CM-H2DCFDA	Thermo Fisher Scientific	Cat# C6827
Nonyl Acridine Orange	Thermo Fisher Scientific	Cat# A1372
TRIzol Reagent	Thermo Fisher Scientific	Cat# 15596018
4% paraformaldehyde, PFA	Dingguo, China	Cat# AR-0211
Triton X-100	Sigma-Aldrich	Cat# T9284

(*Continued on next page*)

Continued

REAGENT or RESOURCE	SOURCE	IDENTIFIER
Critical Commercial Assays		
KAPA HyperPrep Kit	Kapa Biosystems	Cat# KK8504
Annexin V-EGFP Apoptosis Detection Kit	Vigorous Biotechnology	Cat# A002
In Situ Cell Death Detection Kit, POD	Roche	Cat# 11684817910
Cell Meter JC-10 Mitochondrial Membrane Potential Assay Kit	AAT Bioquest®, Inc.	Cat# 22801
VECTASHIELD® Antifade Mounting Medium	Vector Laboratories	Cat# H-1000
Deposited Data		
Raw data files and processed data files for RNA-seq	This study	GEO: GSE130664
Experimental Models: Cell Lines		
KGN cell line	Nishi et al., 2001	N/A
Oligonucleotides		
Primers for RT-qPCR, see Table S6	This paper	N/A
si-IDH1-1, targeting sequences: GCATAATGT TGGCGTCAAA	RiboBio Co., Ltd, China	N/A
si-IDH1-2, targeting sequences: GGCCCAA GCTATGAAATCA	RiboBio Co., Ltd, China	N/A
si-NDUFB10-1, targeting sequences: GCCGAAA TGCAGTGGAAGA	RiboBio Co., Ltd China	N/A
si-NDUFB10-2, targeting sequences: GCACGC AAAGAACAGGTAT	RiboBio Co., Ltd, China	N/A
si-PRDX4-1, targeting sequences: GCGACAGA CTTGAAGAATT	RiboBio Co., Ltd, China	N/A
si-PRDX4-2, targeting sequences: GCTGGAA AGCTGAAGTATT	RiboBio Co., Ltd China	N/A
si-NC	RiboBio Co., Ltd China	N/A
Software and Algorithms		
TopHat (version: 2.0.12)	Trapnell et al., 2009	http://ccb.jhu.edu/software/tophat/index.shtml
HTSeq	Anders et al., 2015	https://htseq.readthedocs.io/en/release_0.11.1/
ToppGene	Chen et al., 2009	https://toppgene.cchmc.org/
GSEA (version: 3.0)	Subramanian et al., 2005	http://software.broadinstitute.org/gsea/index.jsp
Image Lab	Bio-Rad	https://www.bio-rad.com/zh-cn/product/imagelab-software?ID=KRE6P5E8Z
ImageJ	NIH	https://imagej.nih.gov/ij/
FlowJo	Flowjo, LLC	https://www.flowjo.com/
Leica LAS AF Lite (version: 2.6.0)	Leica	https://leica-las-af-lite.updatestar.com/
GraphPad Prism 6	GraphPad Software Inc.	https://www.graphpad.com/scientific-software/prism/
SCENIC	Aibar et al., 2017	https://github.com/aertslab/SCENIC
Seurat (version: 1.4.0.14)	Satija et al., 2015	https://satijalab.org/seurat/
scran (version: 1.2.2)	Lun et al., 2016	https://bioconductor.org/packages/release/bioc/html/scran.html
simpleSingleCell (version: 1.2.1)	Lun et al., 2016	https://bioconductor.org/packages/release/workflows/html/simpleSingleCell.html
GENIE3 (version: 1.0.0)	Aibar et al., 2017; Huynh-Thu et al., 2010	https://bioconductor.org/packages/release/bioc/html/GENIE3.html
DESeq2 (version: 1.20.0)	Love et al., 2014	https://bioconductor.org/packages/release/bioc/html/DESeq2.html

LEAD CONTACT AND MATERIALS AVAILABILITY

Further information and requests for resources and reagents should be directed to and will be fulfilled by the Lead Contact Dr. Guang-Hui Liu (ghliu@ioz.ac.cn). This study did not generate new unique reagents.

EXPERIMENTAL MODELS AND SUBJECT DETAILS

Ethical Statement

This study was conducted in accordance with the Principles for the Ethical Treatment of Non-Human Primates and was approved in advance by the Institutional Animal Care and Use Committee of the Institute of Zoology (Chinese Academy of Sciences). The isolation procedure of human granulosa cells was approved by the Research Ethics committee of the Peking University Third Hospital and was conducted in accordance with approved institutional guidelines. Written informed consent was obtained from the donors.

Experiment Models and Biological Samples

All *Macaca fascicularis* were of Southeast Asian origin. The animals were maintained at around 25°C on a 12 hour (h) light, 12 h dark schedule and raised at Xieerxin Biology Resource with accreditation of Laboratory Animal Care accredited facility in Beijing, in compliance with all local and federal laws governing animal research. All the animals were given commercial diet twice a day with tap water *ad libitum* and were fed vegetables and fruits once daily under careful veterinary oversight. Before the experiment, none of the animals had a clinical or experimental history that would affect physiological aging or increase disease susceptibility. Ovarian tissue samples from 4 young cynomolgus monkeys (4-5 years old) and 4 old cynomolgus monkeys (18-20 years old) were collected and processed for scRNA-seq analysis.

hGCs were isolated and purified from Peking University Third Hospital as previously described (Buck et al., 2019; Ferrero et al., 2012; Feuerstein et al., 2007; Hu et al., 2019). Briefly, human follicular fluid was obtained from donors undergoing the assisted reproductive technology procedure due to a sperm quality issue or restricted tubal patency via ultrasound-guided vaginal puncture. The hGCs were isolated from the follicular fluid using density gradient centrifugation at 2000 rpm for 30 min with Human Lymphocyte Separation Medium (TBD Science, Tianjin, China). Following centrifugation, the middle layer was collected and washed with Dulbecco phosphate-buffered saline (GIBCO). After a brief exposure to 0.2% hyaluronidase (Sigma) at 37°C, the cell suspensions were centrifuged at 3000 rpm for 5 min. Then, the purity of isolated hGCs was assessed by immunofluorescence for hGC markers.

Cell Line

KGN cells, a human granulosa tumor cell line (Nishi et al., 2001), were kindly provided by Dr. Yiming Mu from 301 Hospital of PLA in China. The cells were cultured as previously described in DMEM/F12 medium (GIBCO) supplemented with 10% FBS (GIBCO), 100 U/ml penicillin, and 100 μg/ml streptomycin (GIBCO) at 37°C in 5% CO_2. All the cell cultures were tested negative for mycoplasma contamination.

METHOD DETAILS

Single Cell Isolation

Samples were collected separately from each individual at different days. In brief, the animals were anesthetized and perfused with physiological saline, and then the ovaries were isolated and immediately immersed in M2 medium (Sigma M7167). Then, the fat and other adherent tissues were removed under a dissection microscope to obtain a 'clean' ovary. Half of the ovaries per individual were dissected for single cell isolation and collection. We then roughly divided the ovary into cortex and medulla parts, which were minced and then transferred into 1.5 mL tubes. Then, 500 μL 2 mg/ml Collagenase, Type IV (GIBCO 17104-019) was added into each tube and incubated with the minced tissues at 37°C for 20 min with shaking on thermomixer (1000 rpm). The tube was briefly spun at 1000 rpm, and the supernatant was then gently removed. Next, 1 mL 0.25% trypsin was added to each tube and incubated at 37°C for another 20 min on thermomixer (1000 rpm). The tube was briefly spun at 1000 rpm, and the supernatant was then gently removed. Then, 500 μL M2 medium containing 10% BSA was used to stop digestion. The remaining tissues were pipetted 50-100 times to dissociate the cells. The resulting cell suspension was then transferred into a 3.5 cm dish. Oocytes were manually picked under a dissection microscope and transferred to a PBS–BSA drop (with 0.1% BSA added). The oocytes were collected with a maximum number up to 96 per individual due to the cost concern. Then the debris in the remaining cell suspension was removed by fluorescence-activated cell sorting (FACS) (BD FACSAria II) and subjected to further single-cell collection. 323-480 somatic cells (average 386 cells) from each animal were collected. Each cell was placed into an individual PCR tube with lysis buffer and stored at −80°C for subsequent experiments.

Single-Cell RNA-Seq Library Construction and Sequencing

scRNA-seq libraries were constructed according to the STRT-seq protocol with modifications as previously described (Cui et al., 2019; Dong et al., 2018; Gao et al., 2018; Hochgerner et al., 2017; Islam et al., 2011). Briefly, individual oocytes or somatic cells were picked into lysis buffer by mouth pipetting. Then, the mRNA in lysates was reverse transcribed with SuperScript II reverse

transcriptase (Thermo Fisher Scientific, 18064-071), and an 8 nucleotide (nt) cell-specific barcode was added to the cDNA from each cell. Absolute counting of molecules was performed with the 8 nt unique molecular identifiers (UMIs). The synthesized cDNAs from cells with different barcodes were pooled together and amplified with 19-21 (somatic cells) or 13 (oocytes) cycles, followed by fragmentation with Covaris S2 (Thermo Fisher Scientific) and enrichment of fragments of interest via Dynabeads MyOne Streptavidin C1 beads (Thermo Fisher Scientific, 65001). The enriched fragments were constructed into libraries using a KAPA HyperPrep Kit (KAPA, KK8504) and sequenced on an Illumina HiSeq 4000 platform with a 150-bp paired-end read length by Novogene. It should be noted that oligo-dTs priming may have a potential bias toward mRNAs with long poly(A) tails. As poly(A) tail length is often correlated with the translational efficiency of mRNA (Lim et al., 2016; Subtelny et al., 2014), the ''regulation'' of genes (no matter due to altered mRNA copies or poly(A) tail length) we observed may reflect the changes of the gene's protein levels.

RT-qPCR

Total RNA was extracted using TRIzol Reagent (Thermo Fisher Scientific), and 2 μg total RNA was used for cDNA synthesis with reverse transcription master mix (Promega). RT-qPCR was conducted with the iTaq Universal SYBR Green Super Mix (Bio-Rad) on a CFX384 Real-Time PCR system (Bio-Rad). All data were normalized to the 18S rRNA transcript and calculated by ΔCq or ΔΔCq. All RT-qPCR primer pairs are listed in Table S6.

Western Blot Analysis

Western blot was performed as previously described (Wang et al., 2019). Briefly, protein quantification was performed using a BCA Kit. Protein lysates were subjected to SDS-PAGE and subsequently electrotransferred to a polyvinylidene fluoride membrane (Millipore). The membrane was incubated with the indicated primary antibodies overnight at 4°C and HRP-conjugated secondary antibodies, followed by visualization using the ChemiDoc XRS system (Bio-Rad). The quantification was performed with Image Lab software. The antibodies used in this study are shown in the Key Resources Table.

Ovary Tissue Immunostaining

Immunostaining was performed as previously described (Wang et al., 2015, 2016). Briefly, monkey ovaries were fixed with 4% paraformaldehyde (PFA) at 4°C overnight (O/N), washed extensively with phosphate-buffered saline (PBS), soaked in 30% sucrose, embedded in Tissue-Tek O.C.T. Compound (Sakura Finetek, 4583) and frozen. Frozen sections (8 μm) were cut and placed on positively charged slides and stored at −80°C prior to use. Sections were washed by PBS, and the antigen retrieval were performed by microwaving the sections at 98°C in 10 mM sodium citrate buffer (pH 6.0) for three times (5 min each time). After cooling down, the slides were washed three times with PBS and permeabilized with Triton X-100 (0.4% in PBS) for 25 min (followed by denaturation of cellular DNA with 2 M HCl for immunostaining of 8-OHdG), blocked with blocking buffer (10% donkey serum in PBS) for 1 h at room temperature (RT), and stained with primary antibodies overnight at 4°C. Then, after several washes with PBS, the sections were incubated with secondary antibodies for 1 h at RT. Hoechst 33342 (Thermo Fisher Scientific) was used to stain nuclear DNA. After additional stringent washes, sections were mounted with VECTASHIELD Antifade Mounting Medium (Vector Laboratories, H-1000), and images were obtained using a confocal laser-scanning microscope (Leica TCS SP5 II). The mean fluorescence intensities of GPX1 and GSR were measured using the ImageJ software. An average of over 100 oocytes in primordial follicles and an average of over 50 oocytes in primary follicles in total from three independent sections per animal were used for quantification. To measure the mean fluorescence intensities of IDH1, PRDX4 and NDUFB10, over 300 granulosa cells in total from three independent sections for each monkey were used for quantification. For quantification of the percentage of 8-OHdG-, γH2AX- and Ki67-positive cells, over 1000 granulosa cells in total from three independent sections per animal were used. The signal intensity and the number of positive cells were normalized to those of young group. The antibodies used in this study are shown in the Key Resources Table.

Cell Immunofluorescence

Immunofluorescence was conducted as previously described (Wang et al., 2018). Briefly, the cells were fixed with 4% PFA for 25 min, permeabilized with Triton X-100 (0.4% in PBS) for 25 min, incubated with blocking buffer (10% donkey serum in PBS) for 1 h at RT, and stained with primary antibodies overnight at 4°C. Then, the cells were incubated with secondary antibodies for 1 h at RT. Hoechst 33342 (Thermo Fisher Scientific) was used to stain the nuclear DNA. The antibodies used in this study are shown in the Key Resources Table.

Hematoxylin and Eosin (H&E) Staining

H&E staining was performed as previously described (Nichols et al., 2005). Ovaries were sectioned into two equal-sized halves and preserved in 4% PFA. Fixation was followed by a water rinse and subsequent storage in 70% ethanol. The tissues were subsequently embedded in paraffin wax (Fisher Scientific) following immersion in a graded series of alcohols (70%–100%). Embedded tissue was sectioned (5 μm) using a rotary microtome. The sections were adhered to microscope slides and dried at 56°C for 24 h. Next, slides were passed through a series of the clearing agent xylene and rehydrated in a graded series of ethanol (100%, 100%, 100%, 95%, 80%). After a brief wash in distilled water, the slides were incubated with hematoxylin solution. The sections were then washed with running tap water to remove excess hematoxylin. Then, the sections were differentiated in 1% acid alcohol for 30 s and washed with

running tap water for 1 min. This step was followed by an incubation in the eosin counterstain, subsequent dehydration in a graded series of ethanol (80%, 95%, 95%, 95%, 100%, 100%, 100%), and immersion in xylene. Then, the slides were coverslipped with Cytoseal-60 (Stephens Scientific, USA).

Follicle Counting

Follicle counting was performed using the H&E-stained ovary sections as previously described with minor modifications (Atkins et al., 2014; Johnson et al., 2004; Lass et al., 1997; Morita et al., 1999; Wei et al., 2015). Briefly, primordial follicles were characterized as having a compact oocyte surrounded by a single layer of flattened GCs, while primary follicles were identified by the presence of an enlarged oocyte surrounded by a single layer of cuboidal GCs. Secondary follicles were defined as having an enlarged oocyte surrounded by at least a partial or complete second layer of cuboidal GCs but no more than four complete layers of cuboidal GCs. Antral follicles were characterized by the presence of areas of follicular fluid (antrum) or a single large antral space. Follicles at the primordial, primary, and preantral stages of development were deemed atretic if the oocyte was degenerating (convoluted and condensed or fragmented) or absent. In addition, atretic follicles at antral stage were identified by the morphology that the basement separating the oocyte from granulosa cells often thickens to become the glassy membrane, and the granulosa cells are replaced by fibrous material. To avoid counting a follicle twice, the numbers of primordial, primary and secondary follicles were counted in one out of every 10 serial sections and the numbers of antral follicles were counted in one out of every 40 serial sections. The follicle density was calculated by the number of follicles divided by the volume analyzed. Then the percentage of atretic follicles to total follicles (including healthy follicles at each stage and atretic follicles) was calculated.

Masson's Trichrome Staining

The ovary sections were deparaffinized and rehydrated through 100% alcohol, 95% alcohol and 70% alcohol. After a wash in distilled water, the sections were stained with potassium bichromate solution O/N and rinsed with running tap water for 5-10 min. Then, the sections were stained in iron hematoxylin working solution for 10 min. After a rinse in running warm tap water for 10 min, the sections were stained in Ponceau-acid fuchsin solution for 5-10 min. Then, the slides were washed in distilled water and differentiated in phosphomolybdic-phosphotungstic acid solution for 10-15 min or until the collagen was not red. Next, sections were directly transferred (without rinse) to aniline blue solution and stained for 5-10 min. This step was followed by a brief rinse in distilled water and differentiation in 1% acetic acid solution for 2-5 min. After a wash in distilled water, the slides were dehydrated very quickly through 95% ethyl alcohol and absolute ethyl alcohol and cleared in xylene. Finally, the slides were mounted with resinous mounting medium. Fibrosis areas indicated by blue color were quantified with ImageJ software.

TUNEL Staining

The TUNEL staining of apoptotic populations within ovarian tissue was performed on paraffin sections using the *In Situ* Cell Death Detection Kit, POD (Roche) following the manufacturer's protocol. Then the slides were counterstained with hematoxylin solution for visualization of nucleus. Finally, the slides were mounted with resinous mounting medium. Quantification of the percentages of TUNEL-positive cells used over 1000 granulosa cells in total from three independent sections per animal. The number of positive cells was normalized to those of young group.

Knockdown of DEGs in KGN Cells

siRNA molecules specifically targeting the mRNA of *IDH1*, *PRDX4* and *NDUFB10* were purchased from RIBOBIO (China). The sequences of the siRNAs are shown in Key Resources Table. The negative control duplex, which was also provided by RIBOBIO, was not homologous to any mammalian genes and is widely used in knockdown assays (Liu et al., 2014). KGN cells were transfected with a negative control duplex or siRNAs against *IDH1*, *PRDX4* or *NDUFB10* using Lipofectamine 3000 Transfection Reagent (Thermo Fisher Scientific) following the manufacturer's instructions. 48 h after transfection, the cells were collected for RT-qPCR. 72 h after transfection, the cells were collected for Western blotting. Four days after transfection, the cells were treated or untreated with 600 μM H_2O_2 for 8 h and then RNAs were extracted for RNA sequencing. For crystal violet staining, five days after transfection, the cells were treated with the different concentration of H_2O_2 for 24 h and cultured for another three days before staining. For ROS, mitochondrial mass and mitochondrial membrane potential (MMP) analysis, five days after transfection, the cells were treated with 600 μM H_2O_2, and analyzed by flow cytometry 18 h later. For apoptosis analysis, five days after transfection, the cells were treated with 600 μM H_2O_2 and analyzed by flow cytometry 24 h later.

Crystal Violet Staining

Crystal violet staining was performed as previously described (Cheng et al., 2019; Ling et al., 2019; Zhang et al., 2019). The cells were fixed with 4% PFA for 30 min, and then stained with 0.2% crystal violet for 30 min. After several washes with running tap water, the cell culture plates were scanned with photo scanner (Epson Perfection V370). The intensity of the crystal violet staining was quantified by ImageJ software.

Flow Cytometry Analysis

For analysis of apoptosis, cells were collected freshly and stained with Annexin V-EGFP and PI using an Annexin V-EGFP Apoptosis Detection Kit (Vigorous biotechnology). Then, the apoptotic cells were quantified in a BD LSRFortesa flow cytometer. For measurement of cellular ROS, cells were collected and stained with 1 μM CM-H2DCFDA (Molecular Probes, C6827) for 30 min at RT, and then the signals were quantified in a BD LSRFortesa flow cytometer. For measurement of mitochondrial mass, the cells were collected and incubated with 1 μM Nonyl Acridine Orange (NAO) (Thermo Fisher Scientific, A1372) for 30 min at RT and analyzed in a BD LSRFortesa flow cytometer. For analysis of MMP, the cells were stained with Cell Meter JC-10 Mitochondrial Membrane Potential Assay Kit (AAT Bioquest, Inc.) according to the manufacturer's protocol, and analyzed by BD LSRFortesa flow cytometer.

To avoid experimental systematic error, ROS and apoptosis signals of hGC samples from hospital were normalized with the mean signal in each batch of experiment. The simple regression model was used to fit the relationship between experimental signals and ages. The correlation and responding statistical significance were calculated based on the Spearman's rank correlation.

Bulk RNA-seq Library Construction and Sequencing

Total RNA was extracted from 1×10^6 cells using TRIzol Reagent (Thermo Fisher Scientific). 3 μg per sample were constructed into libraries through NEBNext Ultra RNA Library Prep Kit for Illumina (NEB, E7530L) following manufacturer's manuals. Sequencing data were generated on Illumina HiSeq 4000 platform with 150-bp paired-end read length by Novogene.

QUANTIFICATION AND STATISTICAL ANALYSIS

Single-Cell RNA-Seq Data Processing

The template switch oligo (TSO) and poly(A) tail sequences were trimmed from the raw single-cell RNA-seq data, and then the reads with adapters and low-quality bases were removed to obtain clean reads. The clean reads were mapped against the Ensembl *Macaca fascicularis* reference genome (version: Macaca_fascicularis_5.0) using Tophat (version: 2.0.12) (Trapnell et al., 2009). Only the uniquely mapped reads according to UMI numbers were counted using HTSeq (Anders et al., 2015), i.e., reads with the same UMI sequence were counted only once.

The gene expression level *g* in cell *c* was quantified as the transcripts per million (TPM) $TPM_{g,c}$ as the UMI number of gene *g* divided by the total UMI number of cell *c* and then multiplied by 1,000,000. Since the complexity of scRNA-seq libraries was estimated with ~100,000 transcripts, gene expression levels were transformed into $\log_2(\text{TPM}/10 + 1)$, and unless otherwise stated, "expression levels" indicate the transformed TPM in this study. Genes with TPM $\neq$ 0 were defined as expressed genes.

We retained the high-quality single-cell data that met the following three criteria: the rate of uniquely mapped reads aligned against the reference genome was greater than 20%, the number of detected genes was greater than 700, and the number of detected UMI was greater than 3,000 (Figure S1C; Table S1). After the critical filtering process, 2,601 (191 young oocytes, 227 old oocytes, 931 young somatic cells, 1,252 old somatic cells) out of 3,521 cells were retained for downstream analysis, and the median value of mapping rate was 48.0% and the median number of genes detected in each cell was 1,862.

Identification of Cell Types and Cell Type-Specific Markers

Because of individual variation, we calculated regulation modules based on transcriptional regulators using SCENIC (Aibar et al., 2017), and because there is no transcriptional regulator database for the *Macaca fascicularis* and the genome of *Macaca fascicularis* is similar to the human genome, we used the human hg19 transcriptional regulator database for the SCENIC analysis. We used the UMI counts of 2,601 cells to perform the SCENIC analysis. There were 1,797 transcriptional regulators in the hg19 database, and 1,539 transcriptional regulators were detected in the *Macaca fascicularis* known gene set. We then clustered cells using the SCENIC output file '3.7_binaryRegulonActivity_noDupl.RData' with the modified 'clustering-and-classification' algorithm (Lake et al., 2016). The algorithm was slightly modified, i.e., overdispersed genes were not chosen, and all regulons were used to perform unsupervised clustering. Then, we visualized a *t*-SNE plot using the SCENIC output file '4.1_tsneBinaryActivity_50PC.Rdata'.

We used a standard area under the curve (AUC) classifier to identify cell type-specific markers (DEGs among different cell types) with the function *FindAllMarkers* in the R package *Seurat* (Satija et al., 2015). Markers were selected only if the average difference of the $\log_2$-transformed TPM was greater than 0.5, with a corresponding *power* value greater than 0.25 and a percentage of expressed cells (TPM $\neq$ 0) greater than 30%. GO analysis of cell type-specific markers was performed with ToppGene (Chen et al., 2009). We selected GO terms representing the function of each cell type with P *value* < 0.05 among top 30 terms (Figure 1H).

Identification of Oocyte Subtypes and Subtype-Specific Markers

During calculations, SCENIC performs well in the identification of cell types with high heterogeneity but performs poorly in the identification of cell subtypes with low heterogeneity (Aibar et al., 2017). We identified 418 oocytes based on the SCENIC analysis and then identified oocyte subtypes using expression data normalized by mutual nearest neighbors (MNN) (Haghverdi et al., 2018). We applied MNN correction using the function *mnnCorrect* in the R package *scran* with the parameters '*cos.norm.in = TRUE, cos.norm.out = TRUE, var.adj = TRUE, k = 4, sigma = 0.1*' (Lun et al., 2016). Then, we clustered oocytes using the modified 'clustering-and-classification' algorithm as described above based on the correction data. To construct the oocyte development trajectory, PCA was performed using the R function *procomp* with the correction expression data.

Given the variation in coverage and sequencing depth among different scRNA-seq libraries, we normalized UMI counts with the ERCC spike-in using the R package *simpleSingleCell* (Lun et al., 2016). In brief, UMI counts of endogenous genes were corrected with the function *computeSumFactors*, and UMI counts of the ERCC spike-in were corrected with *computeSpikeFactors*. Then, the $\log_2$-transformed UMI counts were calculated with the size factors.

The AUC classifier was also used to identify oocyte subtype-specific markers with the function *FindAllMarkers* in the R package *Seurat* based on correction data. The maximum expression level of the identified markers should exist in the corresponding defined cluster. We selected the top-ranked genes with a corresponding *power* value greater than 0.4 as the subtype markers. GO analysis of oocyte subtype-specific markers was performed with ToppGene, and GO terms representing the function of each cell type with the criterium of *P value* < 0.05 were selected and terms were ranked the top 30 (Figure 3D).

In the identification of DEGs between consecutive stages, we set the average difference to be greater than 0.005 and *power* to be greater than 0.4.

Aging-Associated Transcriptional Variation Analysis

To observe the aging effects on different cell types, we performed age-relevant coefficient of variation analysis, as described in a previous study (Salzer et al., 2018). We identified highly variable genes (HVGs) using the R package *Seurat* with the parameters '*x.low.cutoff = 0.01, x.high.cutoff = 10, y.cutoff = 0.01*', and we selected the top-ranked 10% genes as HVGs (2,104 HVGs out of 21,040 genes) based on the average expression and dispersion for the downstream aging-associated transcriptional variation analysis.

We defined the cell-paired-distance $d_{c,x}$ for HVG x in cell type c (consisting of y cells from young individuals and o cells from old individuals) as:

$$d_{c,x} = \left| x_{c,i} - x_{c,j} \right|;\ \forall x \in HVG; i \in \{1, 2, \ldots, y\}, j \in \{1, 2, \ldots, o\}$$

Then, we calculated the arithmetic mean of $d_{c,x}$ as $\mu_{c,x}$ and the standard deviation of $d_{c,x}$ as $\sigma_{c,x}$. Therefore, the coefficient of variation of cell-paired-distance, aging-associated transcriptional variation, is defined as:

$$CV_{c,x} = \frac{\sigma_{c,x}}{\mu_{c,x}} \times 100$$

Identification of Aging-Associated Differentially Expressed Genes

To identify aging-associated DEGs between old and young individuals in each specific cell type, the function *FindMarkers* in the R package *Seurat* was used based on t test. Only genes with an average $\log_2$-transformed difference greater than 0.5, a *P value* less than 0.05 and a percentage of expressed cells greater than 70% were considered as aging-associated DEGs. GO analysis of aging-associated DEGs was performed with ToppGene (Figure 5C).

GO enrichment items between young and aged samples were obtained based on the gene set enrichment analysis (GSEA) (Figures 4C and S4E). Briefly, GSEA was performed using the Java software *GSEA* (version: 3.0, desktop application) based on the dataset 'C5 (GO gene sets)' (Subramanian et al., 2005). Hits (gene set numbers) and missed (non-members) were scored with the '*weighted*' enrichment statistic method, and the metric for ranking genes was selected with the '*Signal2Noise*' method. To ensure reproducibility, the random seed in the permutations process was set as '*19961109*'. All the other parameters to perform GSEA were default.

We showed GSEA terms in Figure 4C with nominal *P value* < 0.05 and false discovery rate (FDR, *q* value) < 0.1, and listed the top-ranked 10 terms based on the normalized enrichment score (NES). For Figure S4E, top-ranked 10 NES-based-ranked GSEA terms with *P value* < 0.05 and FDR < 0.2 were shown.

Transcriptional Regulatory Network Analysis

To identify the potential key transcriptional regulators in specific biological processes, based on the expression data normalized by UMI, we performed regulatory network analysis using the R package *GENIE3* (Aibar et al., 2017; Huynh-Thu et al., 2010). We used aging-associated DEGs as input for network analysis and to construct the network between aging-associated transcriptional regulators and targets. Only the transcriptional regulator-target connected with a high weight was retained and used for the network analysis.

For visualization of the network, the node size indicated the number of connections and the line size indicated the weight of a connection; and nodes were ranked based on the node size (Figures 4E, 5G, S3F, S5, and S6A).

Bulk RNA-Seq Data Processing

Raw RNA-seq reads contaminated with adapters and reads with low-quality bases were discarded to obtain the clean reads, and then clean reads were mapped against UCSC human reference hg19 using Tophat, and uniquely mapped reads were counted using HTSeq. Gene expression levels were quantified with RPKM (reads per kilobase million).

DEGs were identified with the R package *DESeq2* (version: 1.20.0) (Love et al., 2014), and we calculated Benjamini & Hochberg FDR to obtain the statistical significance of DEGs. Genes were selected as DEGs only if the $\log_2$-tranformed fold change was greater

than 0.5 (Figure S6I) or 1 (Figures 6I and S6G) with *P value* and FDR both less than 0.05. GO analysis of DEGs was performed with ToppGene (Figure 6I).

Statistical Analyses

The experimental data were statistically analyzed using a one-tailed (Figure 1A) or two-tailed (all others) t test to compare differences between different groups and treatments assuming equal variance with PRISM software (GraphPad 6 Software). A $P\ value < 0.05$ was considered statistically significant. In all figures, one, two and three asterisks indicate $^{*}p < 0.05$, $^{**}p < 0.01$ and $^{***}p < 0.001$, respectively; ns indicates not significant.

Correlation and corresponding statistical significance were calculated based on Spearman's rank correlation coefficient (ρ) in R language (Figures 6B and 6C).

The bioinformatics data were statistically analyzed using a two-tailed t test with R language, and *P value*s were indicated in each figure.

The boxplot represents the median, the first quartile and the third quartile of values; and the whisker represents 1.5 times the interquartile distance. Data in bar plots are shown as the mean ± SEM.

DATA AND CODE AVAILABILITY

The accession number for the raw and processed RNA-seq data reported in this paper is GEO: GSE130664. Publicly available software used in this study are listed in the STAR Methods and the KEY RESOURCES TABLE.

A

No.	Species	Sex	Animal Symbol	Age (Year)
1	*Macaca fascicularis*	Female	YF1	5
2	*Macaca fascicularis*	Female	YF2	5
3	*Macaca fascicularis*	Female	YF3	5
4	*Macaca fascicularis*	Female	YF4	4
5	*Macaca fascicularis*	Female	OF1	18
6	*Macaca fascicularis*	Female	OF2	19
7	*Macaca fascicularis*	Female	OF3	19
8	*Macaca fascicularis*	Female	OF4	20

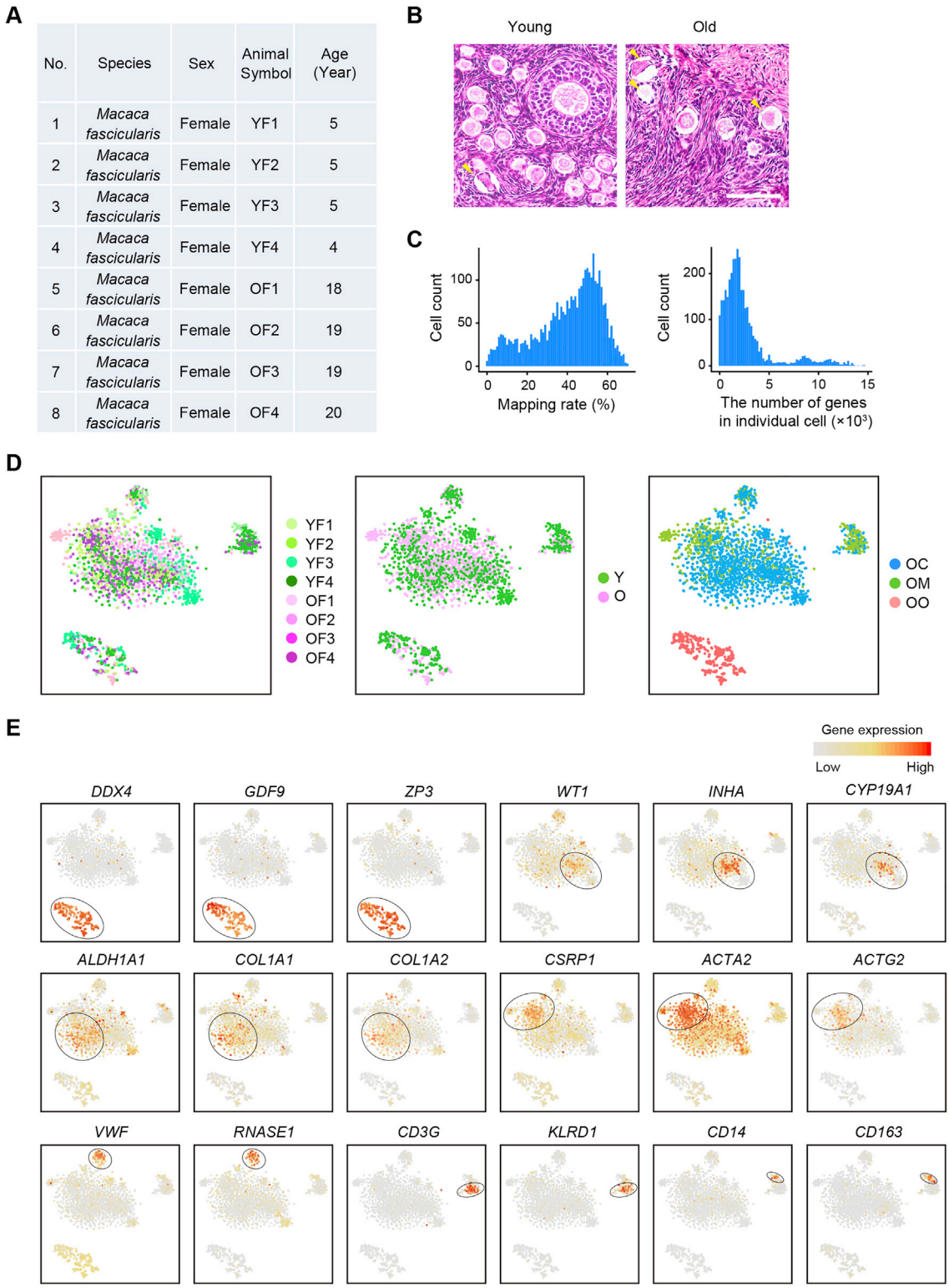

Figure S1. Information on Monkeys and Quality Control of Single-Cell RNA-Seq, Related to Figure 1

(A) Information summary of the monkeys analyzed in this study.

(B) H&E-stained sections of young and old monkey ovaries. Yellow arrowheads indicate the atretic follicles. Scale bar, 100 μm.

(legend continued on next page)

(C) Histogram showing the rates of reads uniquely mapped against the reference genome (left) and the number of genes detected in individual cells (right). These results show the basic quality control of ovarian scRNA-seq before cell filtering.
(D) *t*-SNE plots showing the distribution of single cells from different individuals (left), age groups (middle) and sampling regions (right). No obvious differences in distribution were observed among these features. OC, somatic cells from ovarian cortex; OM, somatic cells from ovarian medulla; OO, oocytes.
(E) *t*-SNE plots showing expression levels of known and newly identified marker genes in distinct ovarian cells.

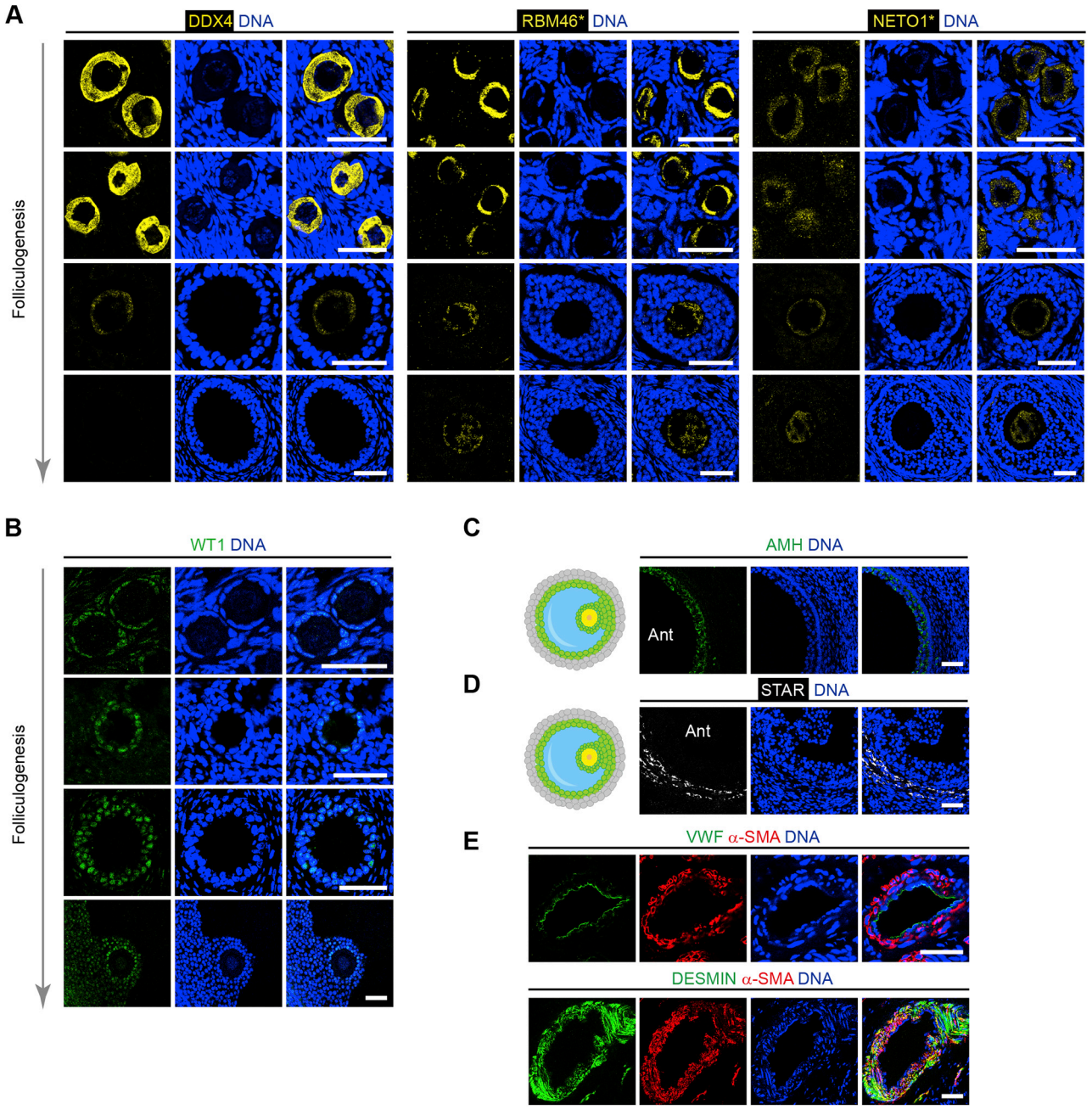

Figure S2. Verification of Different Ovarian Cell Types by Immunofluorescence, Related to Figures 1 and 2

(A) Immunofluorescence analysis of known marker DDX4 for oocytes, as well as novel markers RBM46 and NETO1, which were dominantly expressed in oocytes at different stages of folliculogenesis, and marginally expressed in other somatic cells. Asterisks represent the newly identified oocyte markers. Scale bar, 50 μm.

(B) Immunofluorescence analysis of classic marker WT1 for GCs in the ovary. Scale bar, 50 μm.

(C) Immunofluorescence analysis of classic marker AMH for GCs in the ovary. Scale bar, 50 μm.

(D) Immunofluorescence analysis of the canonical marker STAR for theca cells in the ovary. Scale bar, 50 μm.

(E) Immunofluorescence analysis of classic markers for ECs and SMCs in the ovary, including VWF, DESMIN encoded by *DES* and α-SMA encoded by *ACTA2*. Scale bar, 50 μm.

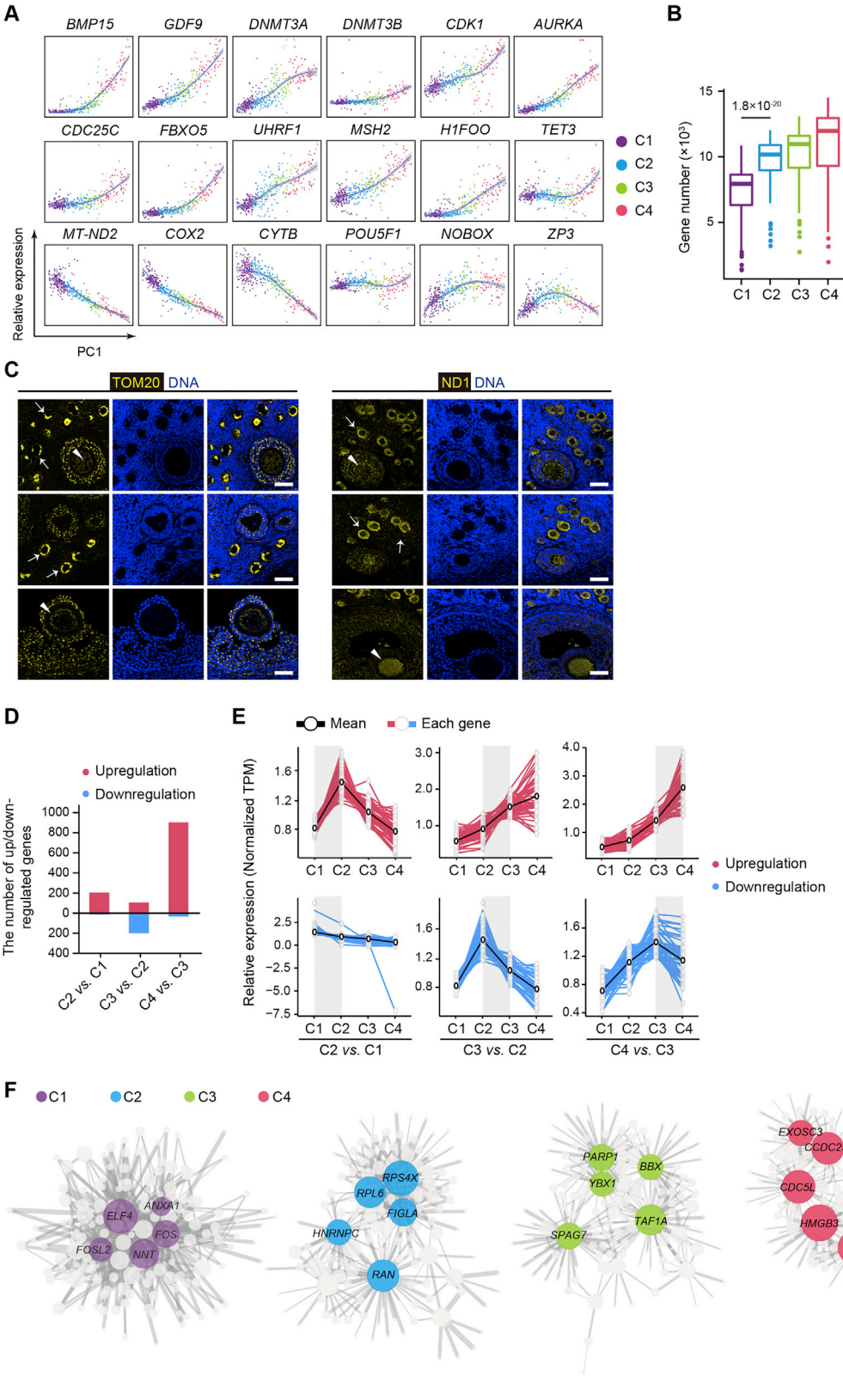

(legend on next page)

Figure S3. Dynamic Gene Expression Patterns and Transcriptional Features in Oocyte Subtypes, Related to Figure 3

(A) Relative gene expression patterns of representative genes essential for oocyte development and maturation along the PC1 dimension.

(B) Boxplot showing the number of expressed genes in each oocyte subtype. Two-tailed t test *P value* is indicated. The number between oocytes C2 and C3, and the number between oocytes C3 and C4 are not significantly different.

(C) Immunofluorescence showing the higher expression levels of the mitochondrial markers TOM20 and ND1 in oocytes at early developmental stages than those in oocytes of late development stages. Arrows indicate primordial and primary follicles, and arrowheads indicate secondary and antral follicles. Scale bar, 100 μm.

(D) Histogram showing the number of upregulated or downregulated DEGs between each consecutive oocyte subtype (DEGs between C2 and C1 oocytes, between C3 and C2 oocytes, and between C4 and C3 oocytes).

(E) Line plots showing expression patterns of top 50 upregulated or downregulated DEGs between two consecutive oocyte subtypes during oocyte development. These DEGs are collected from each gene set shown in Figure S3D. Each line corresponds to each DEG; red lines correspond to upregulated DEGs and blue lines correspond to downregulated DEGs in each consecutive oocyte subtype, and black lines indicate the mean expression level of corresponding DEGs.

(F) Regulatory networks visualizing potential key transcriptional regulators in each oocyte subtype. Only connections with a high weight were retained. The node size indicates the number of connections and top 5 nodes are highlighted. The line size indicates the weight of a connection.

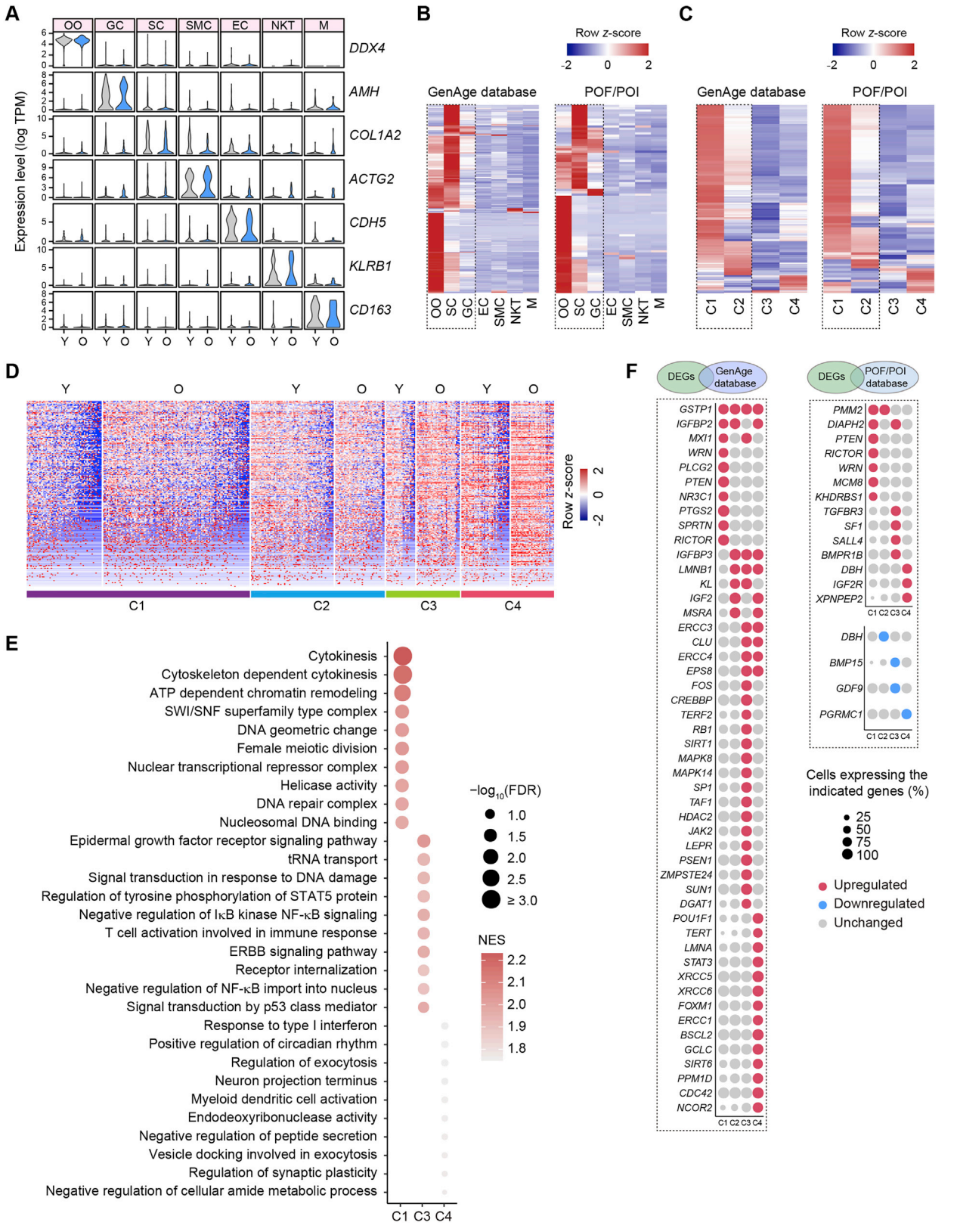

(legend on next page)

Figure S4. Integrative Analysis of Aging-Associated Differentially Expressed Genes with Genes from GenAge or POF/POI Database, Related to Figure 4

(A) Violin plots showing expression levels of marker genes for each cell type in young (Y) and old (O) monkey ovaries.

(B) Heatmaps showing the scaled expression patterns of genes in the GenAge database (left) or of hotspot genes for POF/POI (right) in different cell types.

(C) Heatmaps showing the scaled expression patterns of genes in the GenAge database (left) or of hotspot genes for POF/POI (right) in different oocyte subtypes.

(D) Heatmap showing the scaled expression patterns of meiosis-related genes in different oocyte subtypes obtained from young and old ovaries.

(E) Representative GO terms of upregulated enrichment between old and young monkeys in each oocyte subtype. Functional enrichment was performed by GSEA. The top 10 terms for each subtype were listed based on the normalized enrichment score (NES). The nominal *P value* < 0.05 and FDR (*q* value) < 0.2.

(F) Dot plots showing the expression patterns of overlapping genes which were upregulated or downregulated in each aged oocyte subtype and also included in the GenAge (left) or POF/POI database (right). The circle size indicates percentage of cells expressing the indicated genes. The overlapping upregulated DEGs are colored in red, and the overlapping downregulated DEGs are colored in blue, and other genes are colored in gray.

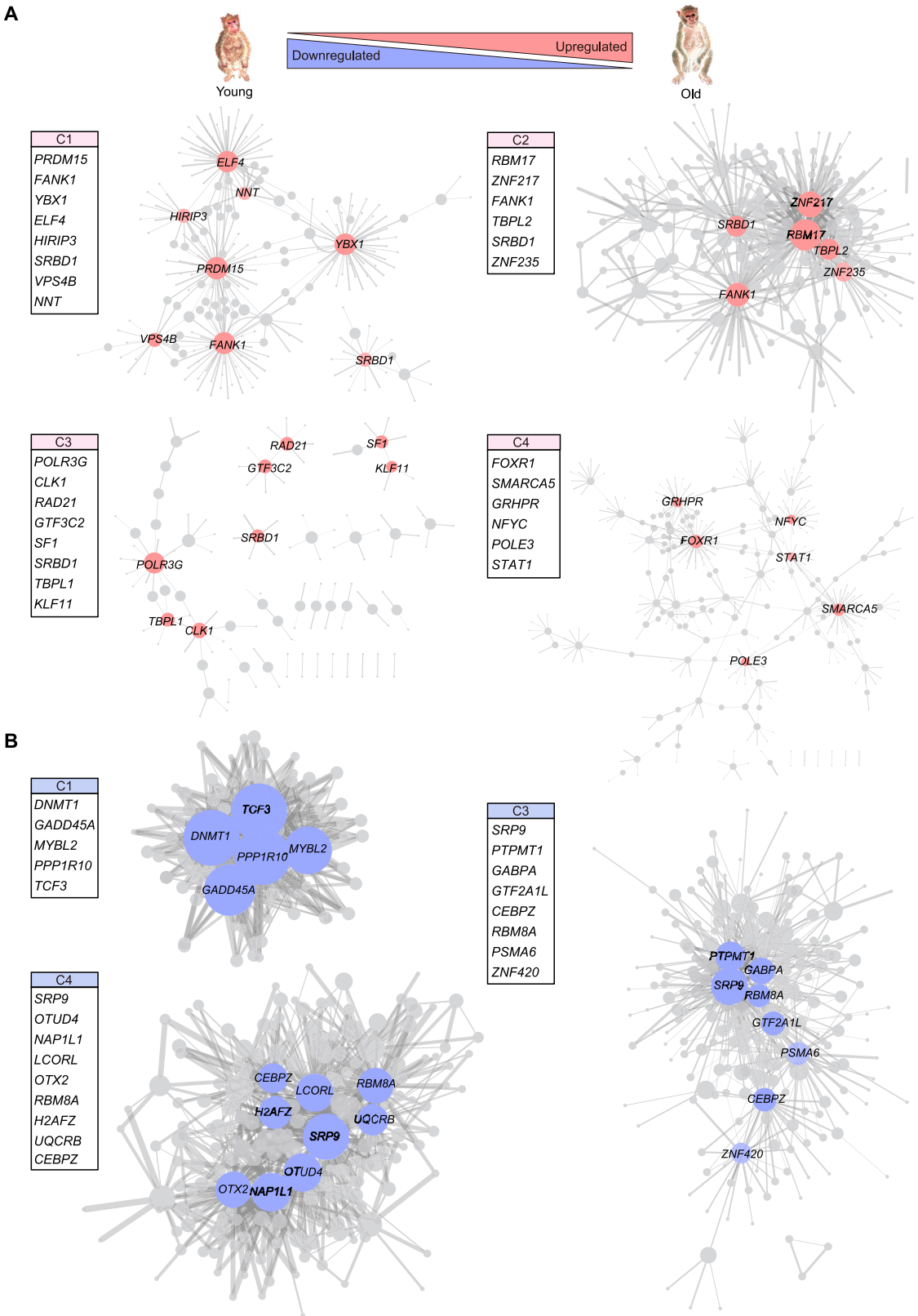

(legend on next page)

Figure S5. Transcriptional Regulatory Network Analysis Uncovering Diverse Aging-Associated Regulatory Modules in Different Oocyte Subtypes, Related to Figure 4

(A) Regulatory networks visualizing potential key transcriptional regulators in upregulated DEGs in each oocyte subtype. Only connections with a high weight were retained. The node size indicates the number of connections, and top-ranked nodes are colored in red. The line size indicates the weight of a connection.

(B) Regulatory networks visualizing potential key transcriptional regulators in downregulated DEGs in each oocyte subtype. Only connections with a high weight were retained. The node size indicates the number of connections, and top-ranked nodes are colored in blue. The line size indicates the weight of a connection.

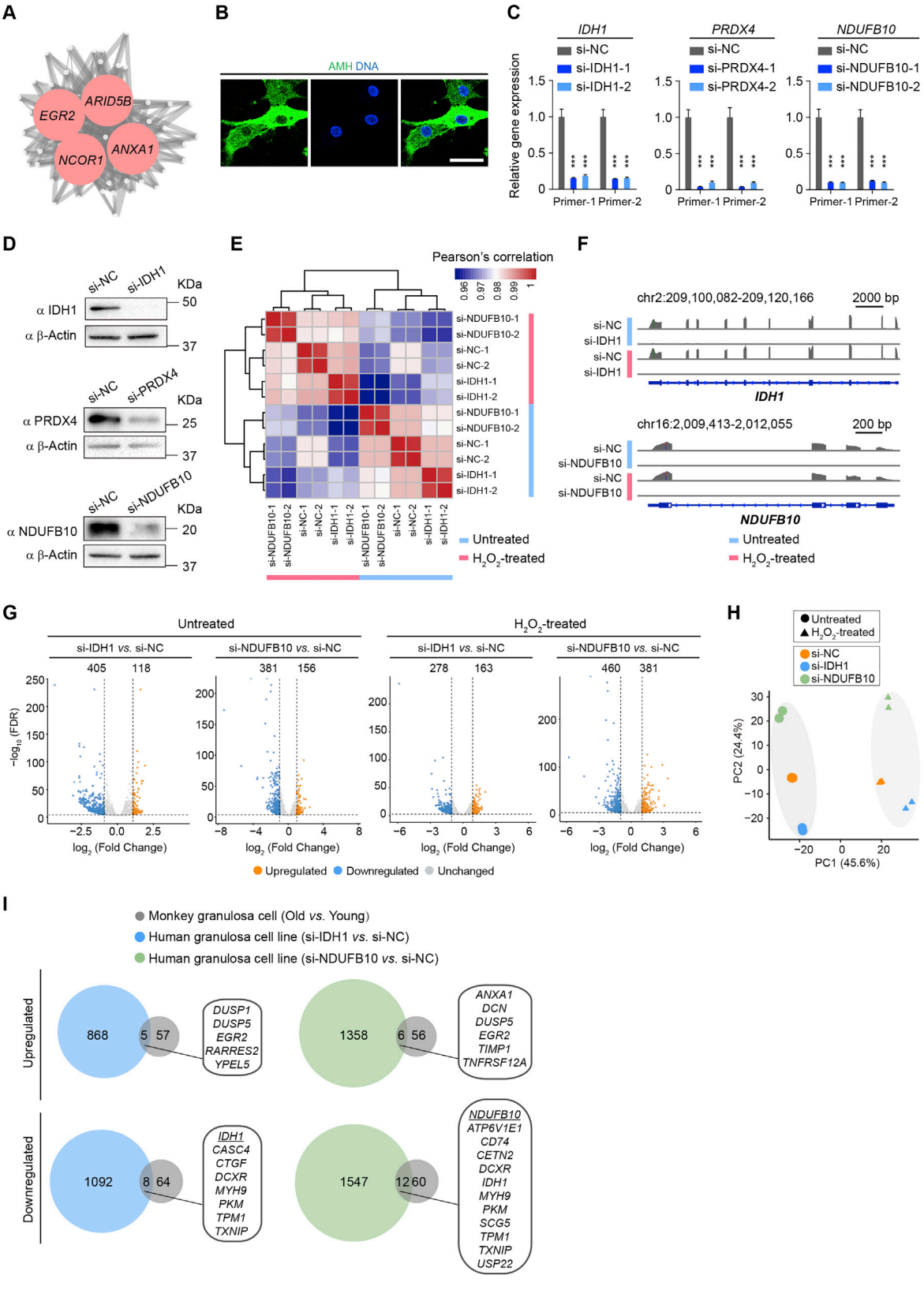

(legend on next page)

Figure S6. Knockdown of Antioxidant Genes in a Human Granulosa Cell Line, Related to Figure 6

(A) Regulatory network visualizing potential key transcriptional regulators in upregulated DEGs in aged GCs. Only connections with a high weight were retained. The node size indicates the number of connections and top-ranked nodes are colored in red. The line size indicates the weight of a connection.

(B) Immunofluorescence analysis of the granulosa cell marker AMH in freshly purified hGCs. Scale bar, 10 μm.

(C) Verification of knockdown efficiency by RT-qPCR, 48 h after transfection with negative control (NC) duplex and siRNAs against *IDH1*, *PRDX4* or *NDUFB10* in KGN cells. 18S rRNA was used as loading control. Data are presented as the mean ± SEM, n = 4, ***$p < 0.001$ (two-tailed t test).

(D) Verification of knockdown efficiency in KGN cells by western blot analysis, 72 h after transfection with NC duplex or siRNAs (siRNA cocktails with siRNA-1 and siRNA-2) against *IDH1*, *PRDX4* or *NDUFB10* in KGN cells. β-actin was used as the loading control.

(E) Heatmap showing the Pearson's correlation coefficient among different samples based on gene expression levels. Replicates indicated high reproducibility, and H_2O_2-treated or untreated groups were clustered together.

(F) The Integrative Genomics Viewer (IGV) snapshots showing RNA reads coverage of *IDH1* or *NDUFB10* indicated efficient knockdown of these two genes.

(G) Volcano plots showing DEGs between the cells transfected with negative control duplex or with siRNAs against *IDH1* or *NDUFB10* in the absence (untreated, left) or in the presence of H_2O_2 (H_2O_2-treated, right). The number of DEGs are shown above the plots. DEGs were identified by $|\log_2(\text{fold change})| \geq 1$ and both the *P value* and FDR were less than 0.05.

(H) PCA showing different samples based on the gene expression patterns exhibited by PC1 and PC2. The variations of PC1 and PC2 are 45.6% and 24.4%, respectively. Distinct samples are shown in different colors. H_2O_2-treated or untreated groups were clustered together and highlighted in gray ellipses.

(I) Venn plots showing the number of overlapping upregulated/downregulated genes between aging-associated DEGs in monkey GCs via scRNA-seq analysis and DEGs after knockdown of *IDH1* or *NDUFB10* in KGN cells upon H_2O_2 treatment using bulk RNA-seq analysis. The overlapping genes are shown in round rectangles. The $\log_2$-transformed fold change of DEGs was greater than 0.5 for both scRNA-seq and bulk RNA-seq. *IDH1* and *NDUFB10* are denoted with underlines.